EINDHOVEN UNIVERSITY OF TECHNOLOGY

Eindhoven University of Technology

MASTER

Designing an in situ fast grating infrared spectroscope, and Argon-Oxygen plasma treatment of SiOxCyHz films

Klaver, A.

Award date:
2001

Link to publication

Disclaimer
This document contains a student thesis (bachelor's or master's), as authored by a student at Eindhoven University of Technology. Student theses are made available in the TU/e repository upon obtaining the required degree. The grade received is not published on the document as presented in the repository. The required complexity or quality of research of student theses may vary by program, and the required minimum study period may vary in duration.

General rights
Copyright and moral rights for the publications made accessible in the public portal are retained by the authors and/or other copyright owners and it is a condition of accessing publications that users recognise and abide by the legal requirements associated with these rights.

- Users may download and print one copy of any publication from the public portal for the purpose of private study or research.
- You may not further distribute the material or use it for any profit-making activity or commercial gain

Eindhoven University of Technology
Department of Physics
Equilibrium and Transport in Plasmas

Designing an *in situ* fast grating infrared spectroscope, and Argon/Oxygen plasma treatment of $SiO_xC_yH_z$ films.

Arjen Klaver

October 2001

VDF/NT 01-13

Advisors:
ir. M.F.A.M. van Hest,
prof. dr. ir. M.C.M. van de Sanden

CONTENTS

1 Introduction **1**

2 Experimental setup **3**
2.1 Fourier transform infrared spectroscopy . . . 3
2.2 Ellipsometry . . . 5
2.3 Deposition and treatment setup . . . 5

3 Design of the fast grating infrared spectroscope **11**
3.1 General grating theory . . . 11
3.2 Optics setup . . . 13
3.3 Mechanical and electronical setup . . . 17
3.4 Resolving power / Timescales . . . 19
3.5 Signal to noise ratio . . . 22
3.6 Summary . . . 26

4 Results and Discussion **28**
4.1 Post deposition treatment . . . 28
4.1.1 General introduction to the results . . . 28
4.1.2 Film properties versus time . . . 31
4.1.3 Film properties versus oxygen flux . . . 36
4.2 Fast grating infrared spectroscopy . . . 42
4.2.1 Gas/reflection . . . 42
4.2.2 Deposition . . . 46
4.2.3 ATR . . . 50

5 Conclusions and Future directions **53**
5.1 Post deposition treatments . . . 53
5.2 FGIR . . . 53

Abstract

At the ETP group at the Eindhoven University of Technology research has been done on deposition of SiO_x-like films with a cascaded arc setup. With this setup it is possible to deposited these films up to 300 nm/s. The drawback of the technique used is that there is a large Carbon concentration in the deposited films. It is believed that this Carbon deteriorates the properties of the SiO_x-like film. In order to improve the deposition, the growth process of the SiO_x film is investigated. A new analysis tool has been developed to monitor *in-situ* the initial film growth; this tool is called the Fast Grating InfraRed (FGIR) spectroscope. With this spectroscope an infrared absorption spectrum of the film can be measured every 2.9 ms. From the infrared absorption spectrum, the various material bonds in the film can be identified, and this will provide information about the growth process of the SiO_x-like films.

The designed FGIR setup can measure infrared absorptions between 7 μm and 14 μm, with a resolution of 0.08 μm. The resolving power is about 40 and the sensitivity of the setup is 30 nm with a Silicon sample as substrate. If an ATR crystal is used as substrate for the film, the sensitivity of the setup is improved, and 2 nm film absorptions can be detected.

Also the possibility of improving the SiO_x-like films by a post deposition treatment has been investigated. This treatment involves exposing the deposited SiO_x films to an Argon/Oxygen plasma, and the atomic Oxygen is this plasma reacts with the Carbon or Carbon related groups in the film, and a volatile species is created, which is removed from the film. For thin films (<300 nm) it was found it is possible to remove most of the Carbon within 5 minutes of treatment. If the films become thicker the oxygen has to diffuse through a thicker film to get the Carbon out and it has been found that this diffusion is a slow process. With the treatment not only Carbon is removed from the film but also more Oxygen is build into the film. Finally it has to be noted that for the ETP setup the atomic oxygen flow at the surface of the sample is not linear with the molecular oxygen flow at the nozzle of the cascaded arc. It was found that when increasing the molecular oxygen flux at the nozzle, this could even decrease the atomic oxygen flow at the substrate. This effect was contributed to the larger diffusion coefficient of the atomic oxygen compared to the diffusion coefficient of the Argon ions in the plasma.

1. INTRODUCTION

In the industry there is much interest in the deposition of thin Silicon Oxides (SiO_x) and SiO_x-like films. SiO_x materials are hard, transparent, resistant to many chemical attacks, and are non-conductive, and therefore these materials have many uses. They can be used for instance as a non conductive layer between conducting layers in metal-insulator-semiconductor structures in the semiconductor industry. Another important field of use for the SiO_x films is as a coating for various applications. SiO_x coatings can be used to passivate electronical circuits to make them more resistant to chemical and mechanical attacks. They can be used to harden other transparent materials against scratches. Also the coating can be used in the packaging industry to produce new ecological barriers.

For the deposition of coatings it is often important that the substrate temperature is low, typically below 300 $°C$, otherwise the substrate can deteriorate under the high temperatures. Three different approaches have been used to deposit these layers with low substrate temperatures: Plasma Enhanced Chemical Vapour Deposition (PE-CVD) [Adam83], photo CVD [Numa83], and Remote Plasma Enhanced CVD (RPE-CVD) [Rich85].

As precursor for the deposition of the SiO_x or SiO_x-like various chemicals have been used. The most straightforward technique utilizes Oxygen diluted Silane plasmas [Luco83]. But then stringent safety measures need to be taken, while Silane is highly toxic and explosive. Therefore there is a tendency to work with organic precursors like TEOS (Tetraethylorthosilica) [Char92], TMOS (Tetramethoxysilane) [Boga95], and HMDSO (Hexamethyldisiloxane) [Thei94], which require less safety restrictions. The drawback of these precursors over Silane is that the films can contain more contaminations such as Carbon and Hydrogen.

At the ETP group at the Eindhoven University of Technology (EUT) research has been performed on the RPE-CVD deposition of SiO_x coatings with HMDSO as precursor [Mitu99]. The remote plasma setup makes it possible to separate the processes of plasma generation, transport of the plasma, and deposition from each other. As a plasma source a DC cascaded arc is used, and high deposition rates have been obtained with this kind of setup and plasma source [Graa00] [Mitu99].

Technology assessment

The SiO_x films deposited with the ETP setup have a large Carbon concentration and therefore must be qualified as SiO_x-like (or $SiO_xC_yH_z$) materials. It is this Carbon that is unfavorable to the material properties of the SiO_x film for several applications. In this master thesis two methods are introduced to reduce the Carbon content in the SiO_x-like films; one direct way and one indirect.

The first method involves a plasma treatment after the films are deposited. These treatments have been called post deposition treatments. It is believed that when exposing the SiO_x-like films to an Argon/Oxygen plasma, the Oxygen radicals in the plasma would react with the Carbon in the film and the Carbon can be removed from the film by such a reaction. Here several questions about the reacting particle, the transport mechanism and the reactions

inside the layers need to be answered to get a better understanding of the treatment.

The other method of reducing the Carbon content in the SiO_x-like films is of an indirect way. A new analysis tool has been designed to study the initial growth of the SiO_x-like film, and from this kind of studies more information about the reactions and growth mechanism of the films are obtained. With this information better deposition processes can be developed which would then lead to a lower Carbon content in the film and thus a better quality of the film.

Infrared absorption spectroscopy has been chosen for the analysis, because with the technique, the composition and bond types in the SiO_x-like films can be observed *in-situ* during film growth. The films deposited with the ETP setup have a high growth rate and this will limit the measuring time for the absorption spectra, if initial growth (monolayer growth) needs to be measured. The deposition rate of the setup is typically 30 nm/s but this can be up to 300 nm/s. As a result to measure monolayer (3 Å thick) absorptions the measuring time for one spectra needs to be less then 10 ms. With the conventional Fourier Transform InfraRed (FTIR) spectroscopes this would not be possible. A new Fast Grating InfraRed (FGIR) spectroscope was developed to meet the previous conditions.

To be able to meet the stated conditions several special elements have been introduced in the FGIR setup. A high speed optical scanner was used to rotate a grating with speeds up to 300 Hz, with a sufficient rotational angle. The rotation speed of the grating determines the measuring time for one spectrum. To get detectable monolayer absorptions a Attenuated total reflection (ATR) crystal was used. This kind of crystals will increase the path length of the light through the film and this will increase the absorption by at least one order. To have sufficient photons to be detected, a cascaded arc was used, as it is proved that the light emision of the arc in the infrared is much higher then for a conventional glowbar [Have89].

Chapter two of the thesis gives the experimental setup for the deposition tool and the analysis tools used for the post deposition treatment experiments. Chapter three describes each element in the FGIR setup and all the considerations for the elements used. Chapter four gives the results for the post deposition treatments and the preliminary results of the FGIR setup. Also a discussion for the results is given in this chapter. Chapter five gives the general conclusions and the future directions of the research.

2. Experimental setup

2.1. Fourier transform infrared spectroscopy

The Fourier Transform InfraRed (FTIR) spectroscope is an elegant and easy way to obtain an infrared absorption spectrum. It has two advantages over grating spectroscopes. Compared to grating spectroscopes, it has a large energy throughput and it can scan a large spectral range at one time. Its main disadvantage is that takes a long time to measure a spectrum (typically 1 second). It uses a Michelson interferometer which consist of two mirrors and a beam splitter. When one of the mirrors is moved it generates a physical path difference between the both light beams after separation and recombining at the beamsplitter. This path difference will result in interference in the detected signal. With the FTIR a so-called interferogram (irradiance versus path difference) is measured and this is the Fourier transform of the corresponding spectrogram (irradiances versus wavenumber).

To obtain a transmission spectrum of the sample, first a intensity spectrum is measured without the sample in the light beam. Then the sample is put into the FTIR (before or after the actual interferometer) and another intensity spectrum is measured. Then the latter intensity spectrum is divided by the first, and the result is the transmission spectrum of that sample. To get the transmission spectrum of only the film on a substrate, the transmission spectrum of the sample with film is divided by the transmission spectrum of the sample without the film. Figure 2.1 shows the transmission spectrum of a typical SiO_x-like film. Here absorption peaks can be seen on a varying baseline. The baseline is not unity for each wavelength due to interference in the deposited film but sinusoidal.

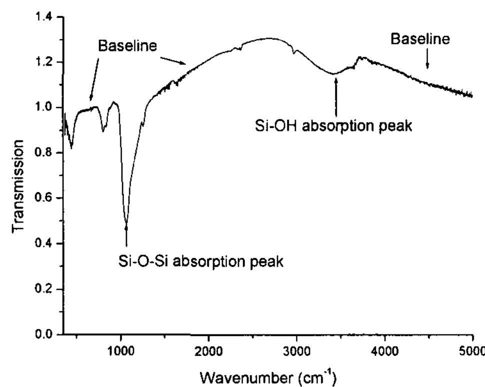

Figure 2.1: *Typical absorption spectrum of a SiO_x-like film measured with the FTIR spectroscope.*

Each absorption peak in the transmission spectrum corresponds to a different molecular vibrational energy transition inside the measured material. Each molecule or bond type in the material has different absorption peaks, and so each absorption peak can be attributed

to a specific bond type in the material, although sometimes the absorption peaks of different materials can overlap. In this way, from the transmission spectra, information on the bond types in the film can be extracted.

If all the absorptions are removed from the spectrum the interference pattern of the film remains. Now is it possible to deduct from this interference pattern the thickness d and the refractive index n_2 of the film [Born99].

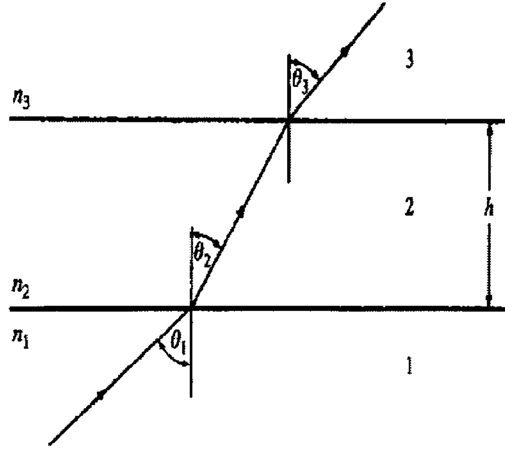

Figure 2.2: *Configuration of layers used to calculated the transmission of the film and the definition of various other parameters used in the calculation.*

Assume the configuration of layers as given by figure 2.2; material 1 with refractive index n_1 is air, 2 with refractive index n_2 is the investigated film, and 3 with refractive index n_3 is the substrate. The incident angle of the light is θ_1 and the other two angles $\theta_{2,3}$ are related to θ_1 by Snell's law. For this configuration the transmission T through the stack can be calculated as a function of the wavelength λ of the light by.

$$T = \frac{1-(R_s+R_p)|_\lambda}{1-(R_s+R_p)|_{\lambda\to\infty}}, \tag{2.1}$$

$$R_{s,p}(\lambda) = |r_{s,p}(\lambda)|^2 = \left.\frac{r_{12}^2+r_{23}^2+2r_{12}r_{23}\cos(2\beta)}{1+r_{12}^2r_{23}^2+2r_{12}r_{23}\cos(2\beta)}\right|_{s,p}, \tag{2.2}$$

$$\beta = \frac{2\pi}{\lambda}n_2 d\cos(\theta_2), \tag{2.3}$$

where $r_{x,y}|_{s,p}$ in equation 2.2 are the Fresnel coefficients for s- or p-polarized light for the corresponding interface between layer x and y. Now the interference spectrum can be fitted by equation 2.1 with as fitting parameters n_2 and d. Note that the thickness d and the refractive index n_2 are dependant in equation 2.3, and therefore have a large dependence in the fitting procedure. To avoid this problem a new parameter is introduced: the optical thickness. This is the refractive index multiplied by the thickness of the layer. This parameter is more rigid to errors in the fitting procedure.

2.2. Ellipsometry

Ellipsometry is used to measure, *in situ*, the thickness and the refractive index of a film during deposition [Tomp93]. It is based on the principle that s- and p- polarized light will reflect different on the sample, and this difference is expressed in the ellipsometry parameters Ψ and Δ. tanΨ is the ratio between the absolute values of the reflection coefficient of the layer for s- and p-component of the light, and Δ is the phase difference between the s- and p-component of the light.

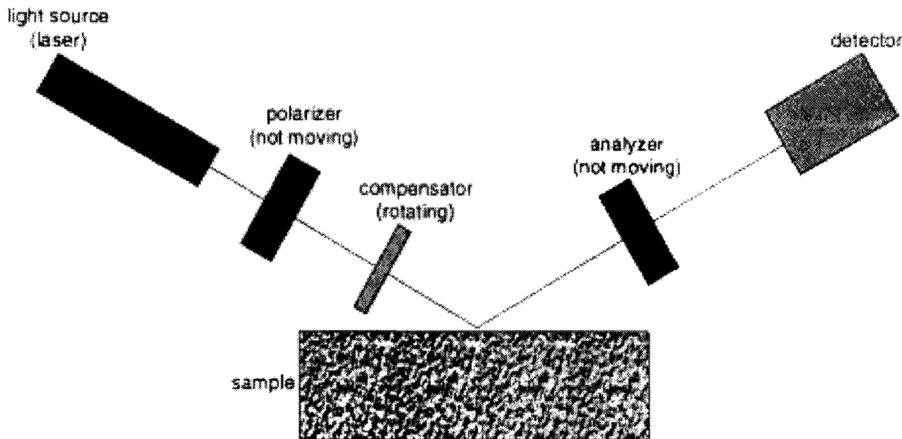

Figure 2.3: *The setup used for the ellipsometry measurements.*

For the measurement a rotating compensator ellipsometer in the polarizer compensator sample analyzer (PCSA) configuration is used as shown in figure 2.3. As a light source a HeNe laser is used. The light is then made elliptical polarized with the polarizer and the compensator (a quarter wave plate), after which the light is reflected off the sample to another polarizer, the so-called analyzer, and after this the intensity of the beam is measured. If ϖ is the rotating frequency of the compensator then the signal on the detector can be written as:

$$I_d = I_0(a_0 + a_2 \cos 2\varpi t + b_2 \sin 2\varpi t + a_4 \sin 4\varpi t + b_4 \sin 4\varpi t) \tag{2.4}$$

where from a_0, a_2, a_4, b_2 and b_4 the parameters Δ and Ψ can be calculated (see Bart Hovens [Hove97]). It is generally impossible to deduce from only one Δ, Ψ point directly the film properties n, k and d and therefore during a deposition Δ and Ψ are measured constantly and a Δ and Ψ trajectory is obtained. Figure 2.4 gives a typical Δ and Ψ-trajectory for a $SiO_xC_yH_z$ film on a Silicon substrate.

When comparing the measured Δ and Ψ-trajectory with a computer simulation, one can obtain the thickness and the refractive index of the film as a function of thickness. But it is possible that two different simulations will result in the same Δ and Ψ trajectory, so often some user intelligence is needed for a correct analyses of the ellipsometry data.

2.3. Deposition and treatment setup

All the plasma assisted SiO_x-CVD experiments as well as the post deposition experiments have been performed with the so-called "depo 1" tool. It is also the tool where the new Fast Grating InfraRed (FGIR) spectroscope has been implemented on to do *in-situ* infrared

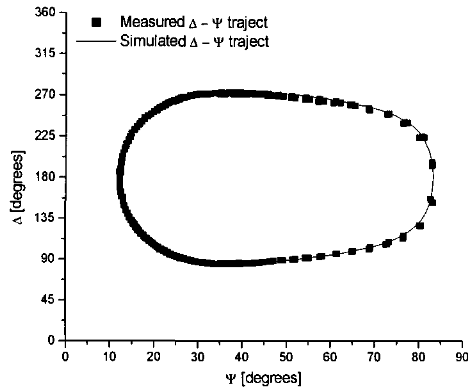

Figure 2.4: *The figure shows the* Δ *-* Ψ *trajectorty for a typical SiO-like film deposition, also and the simulation of the film deposition on a Silicon substrate is shown (n=1.43).*

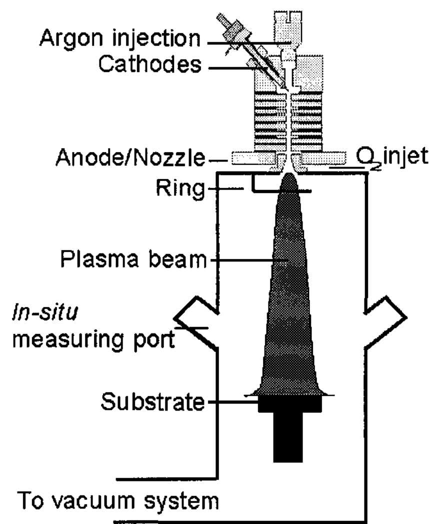

Figure 2.5: *Schematic picture of the experimental setup (depo 1).*

absorption spectroscopy measurements. Depo 1 is a so-called remote plasma setup where the creation of the plasma is spatially separated from the area where the sample resides. For the depositions and the post treatments an Argon/Oxygen plasma was used.

The setup is shown in figure 2.5. As a plasma source a cascaded arc is used, which is an efficient way to generate a plasma with a high ionization degree. The ionization degree can be up to 25%, and the electron temperature is approximately 1 eV [Brus99]. The arc is mounted vertically on top of the vessel and is movable in that direction, i.e. the distance between the arc exit and the substrate can be changed. Argon is injected into the arc at the cathodes, and an Argon plasma is generated in the arc. Due to the large pressure difference between the arc and the vacuum vessel, this plasma exits the arc supersonic at the nozzle. When the plasma leaves the arc, no more energy is injected into the plasma, and the electron temperature decreases rapidly to 0.2 to 0.3 eV. Therefore it is fair to assume that no new Argon ions or excited Argon atoms are created.

The Oxygen is injected into the Argon plasma at the nozzle. When Oxygen is injected in

the plasma the following reactions between the Argon plasma and the Oxygen can occur: The main reactions of the plasma and the molecular oxygen are the charge exchange reaction and the excitation dissociation reaction:

$$Ar^{+} + O_2 \rightarrow Ar + O_2^{+} \quad (2.5)$$

$$Ar^{*} + O_2 \rightarrow Ar + O^{*} + O. \quad (2.6)$$

The rate coefficients for the reaction 2.5 and 2.6 are $5*10^{-11}$ cm^3/s and $2*10^{-10}$ cm^3/s respectively [Rauf97]. The reaction rates between the molecular Oxygen and the electrons in the plasma are at least one order of magnitude lower, due to the low electron temperature, and are here neglected. The O_2^+ created in reaction 2.5 can be further dissociated by dissociative recombination:

$$O_2^{+} + e \rightarrow 2O \quad (2.7)$$

$$O_2^{+} + e \rightarrow O^{*} + O. \quad (2.8)$$

The rate coefficients for reaction 2.7 and 2.8 is $3*10^{-8}$ cm^3/s and $1*10^{-8}$ cm^3/s respectively. These are fast reactions compared to reactions 2.5 and 2.6 and therefore the concentration of O_2^+ will be low compared to O_2 and O. The excited O^* created in reaction 2.6 and 2.8 can fall to the ground state by the following reaction:

$$O^{*} + e \rightarrow O + e. \quad (2.9)$$

Each Argon ion or excited Argon atom can consume one oxygen molecule and this reaction will almost always result in the dissociation of the molecular oxygen into two oxygen atoms. The main loss reactions in the gas phase for the atomic oxygen are:

$$O + Ar^{+} \rightarrow O^{+} + Ar \quad (2.10)$$

$$O + Ar^{*} \rightarrow O^{*} + Ar, \quad (2.11)$$

with a rate coefficient of $6*10^{-12}$ cm^3/s and $4*10^{-11}$ cm^3/s respectively. But the reactions 2.10 and 2.11 are unlikely. The atomic oxygen loss at the wall of the vessel is large, with a rate coefficient of $1*10^{-4}$ cm^3/s. The reaction at the wall is given by:

$$O + O\ (wall) \rightarrow O_2. \quad (2.12)$$

For a low Oxygen flow the atomic oxygen concentration will be small and then the amount of reaction will also be small. Furthermore are the rate coefficients for reaction 2.10 and reaction 2.11 are lower then for the other reactions. For high Oxygen flows, the Argon will be consumed primarily by the oxygen in reaction 2.5 and 2.6 and cannot be used for reaction 2.10 and 2.11. When oxygen ions are created they will not be consumed by another reaction; there is no major loss channel for the O^+.The main particles in the plasma are therefore in order of possible concentration: O, O^*,O_2^+ and O^+ [Rauf97] [Lieb94].

The Argon plasma with the Oxygen injected exits the arc and moves to the substrate. The time of flight of the plasma is one or two milliseconds [Brus99]. A few centimeters outside the arc a stationary shock will occur in the supersonic plasma beam and hereafter the

Table 2.1: The process paramers used for the deposition.

Parameter	Value
precursor	HMDSO
precursor flow	1.98 sccs (25 %)
Precursor carrier gas flow: Argon	1.60 sccs (50%)
Argon flow through arc	25 sccs
Oxygen flow (injected at nozzle)	5 sccs
Current through arc	50 A
Temperature substrate	50 °C
Deposition time	20-30 s

plasma moves subsonic further to the substrate. During a deposition the precursor (Hexamethyldisiloxane, HMDSO) is injected into the plasma through a pierced ring with a diameter of 10 cm, which is mounted 5 cm below the nozzle. The flow of the precursor is controlled with a liquid flow controller in combination with a controlled evaporation module [Boer95], and Argon gas is used as a carrier gas. In the plasma the precursor will dissociate and the dissociated products will move with the plasma to the substrate where they will react to form a film. The distance between the arc and the substrate was approximately 60 cm during the experiments. The substrates are held at a fixed temperature with electrical heaters and liquid nitrogen/watercooling. The heat contact with the substrate is optimized by a helium backflow under the substrate.

On the depo 1 setup a number of analysis tools are available, like Fourier transform infrared (FTIR) spectroscopy, single wavelength ellipsometry, cavity ring down spectroscopy (CRDs), and mass spectroscopy, but only ellipsometry and FTIR spectroscopy have been used. More information on the setup can be found in the Ph.D. thesis of J. Gielen [Giel96] and/or A. de Graaf [Graa00].

Deposition and post deposition treatment experiments

The depositions and the post depositions experiments were performed in the following way: First a Silicon sample was cleaned to remove dust and grease from its surface of the samples, then the transmission spectrum of the sample was *ex-situ* measured in the FTIR spectroscope. After this a 500 to 700 nm thick SiO-like layer was deposited on the sample. The deposition parameters used for the experiment are given by table 2.1 and were kept the same for every deposition. These parameters for the deposition are the so-called *standard condition* for the deposition process, and they have been chosen while they provide good optical properties for the deposited layer as well as have a high deposition rate. In table 2.1, HMDSO is short for hexamethyldisiloxane or $(CH_3)_3$-Si-O-Si-$(CH_3)_3$. More on the deposition process can be found in the ETP internal report of B. Mitu [Mitu99].

During the deposition the growth process of the film was monitored by means of ellipsometry, and the growth rate and the refractive index of the film were measured. After the deposition the samples were again *ex-situ* measured with the FTIR spectroscope and the transmission spectrum of only the deposited SiO_x-like film could be obtained. The samples were then returned to depo 1 for the post deposition treatment.

For the post deposition treatment experiments the samples where exposed to the Argon/Oxygen plasma. Table 2.2 shows the process window for the parameters used for the post deposition treatment experiments.

Table 2.2: The process window for the post deposition treatment.

Post plasma treatment parameters	Value
Substrate temperature	50 $°C$
oxygen flow	0..17 sccs
argon flow	100 sccs
current through arc	75 A
treatment time	0.5..60 minutes

Also during the treatment the films were monitored by means of ellipsometry. After the treatment the samples were then measured again *ex-situ* in the FTIR spectroscope and the new transmission spectrum of the SiO_x-like film is obtained. The spectra before and after the treatment are then compared and changes in the various bond types in the SiO_x-like film have then been noted.

To compare the absorption peaks in the transmission spectra, for each peak the absorption area has been determined. To do this first a straight line is drawn between the left and right top of the absorption. Then the area between the line and the absorption is calculated. The absorption peak area is an indication for the amount of that particular bond type in the measured material. The changes in the peak area before and after the treatment are recorded. The transmission spectra were also used for the measurement of the optical thickness. The method for this is described in section 2.1.

If the peak area could not be calculated, due to overlap of another absorption peak or only part of the absorption peak is measured, then another technique can be used. Instead that the peak are compared by their peak area, the peak is analyzed by the maximum absorption intensity. First the baseline for the absorption peak is calculated, normally this is done by fitting a region near the absorption where no absorption occurs with a straight line. This straight line is then extrapolated over the absorption peak and used as a baseline to determine the absorption intensity of the absorption peak. Then the maximum distance between the transmission spectrum and the straight line is calculated and this is called the maximum absorption intensity.

Heat load experiment

The heat load of the various Ar/O_2 mixtures has been measured to check if the plasma would influence the temperature of the top part of the sample. Although the samples are cooled from the bottom, a temperature gradient can exist over the sample. To discard this possibility heat load experiments were performed.

For the experiment the liquid nitrogen cooling was switched off. Then the plasma was turned on, the current through the arc was set to 75 A and the Ar flow was set to 100 sccs. The oxygen flow at the beginning of the experiment was zero. When the plasma was started the temperature of the substrate began to rise. Every minute the temperature was measured. During the experiment the data was already analyzed and a saturation temperature was extrapolated for the temperature rise from the data. To speed up the experiment, after 80 minutes the temperature was raised by electrical heating to this saturation temperature. Then the heating was switched off again and the temperature was left to stabilize again. Every one minute the temperature was measured again. Regularly the oxygen flow was changed. The temperature course of this part of the experiment is given in figure 2.6.

When the oxygen flow was set to 5 sccs the temperature would drop slowly. When the

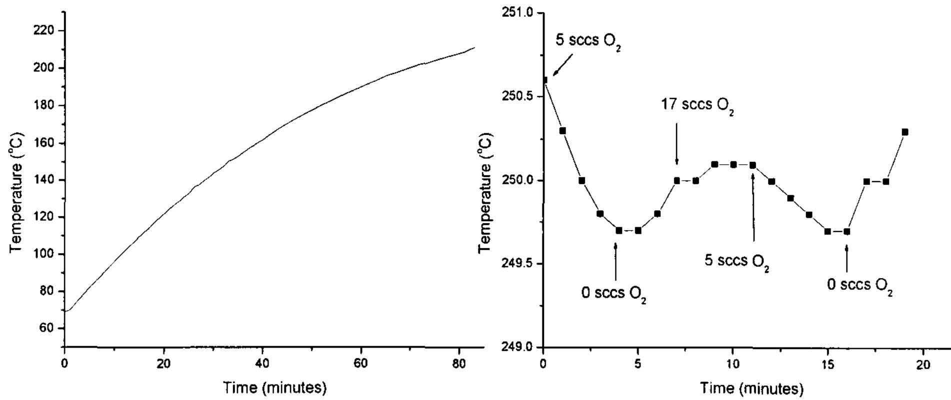

Figure 2.6: *Temperature course during the treatment. On the left the first 80 minutes and on the right the last 20 minutes.*

oxygen flow was set to 0 sccs the temperature would rise, and when the oxygen flow was set to 17 sccs the temperature stayed almost constant. From this course and the comparison with the temperature course at the beginning of the experiment, it was concluded that the equilibrium temperature for the Argon/Oxygen mixture of 100/0 it is slightly above 250 $°C$, but not more then 260 $°C$. The argon/oxygen mixture of 100/5 would lead to a equilibrium temperature of slightly below 250 $°C$, but not less then 240 $°C$ and the 100/17 mixture leads to a temperature of about $250 \pm 0.5 °C$. The difference between the highest and lowest equilibrium temperature is low and so the energy flux to the surface will not exhibit a large difference for various mixtures of the Oxygen/Argon plasma. The temperature gradient across the sample will be the same for all the argon/oxygen mixtures of the plasma, and the temperature of the top of the SiO_x-like film will be in all cases comparable.

3. Design of the fast grating infrared spectroscope

A new infrared absorption setup has been designed to analyze real time the initial growth of SiO_2-like layers. The growth rate of these films with the ETP setup is typically 30 nm/s but this can be up to 300 nm/s [Mitu99]. At this rate, to measure the absorption of only one monolayer (0.3 nm) a measurement must take less then 10 ms. This is impossible with the commonly used Fourier Transform Infrared Spectroscopes (FTIR). A FTIR spectroscope can typically perform a measurement with a reasonable signal to noise ratio in one second [Marc90].

Therefore the more traditional methods of spectroscopy with dispersive elements were considered. Now with the emergence of high speed optical scanners it has become possible to do an absorption measurement with these these kind spectroscopes much faster. These kinds of high speed optical scanners are capable of rotating the dispersive element up to 300 Hz, given the right choice of elements.

Gratings and prism's are two distinct ways to disperse light into their separate wavelengths. As the dispersive element gratings have been chosen because they are in general lighter and therefore is the scanner capable of rotating the grating much faster then if a prism was chosen. Also, in general, the dispersion of the gratings is higher then the dispersion of prism (like CsBr) in the desired wavelength range [Hurt92].

However there are some disadvantages of the grating spectroscopes compared to the FTIR systems. With a grating, the wavelength interval and therefore also the irradiance on the detector will be restricted at any one time. If the same light source is used the intensity on the detector in a grating spectroscope would be a fraction of the total light intensity of the light source. With the FTIR spectroscopes the light intensity on the detector during one measurement would be on average the total light intensity of the light source. Grating spectroscopes put higher demands on the light source then FTIR spectroscopes.

Also the measuring range with gratings are generally less then with FTIR spectroscopes; due to overlap. Often is the measuring range is the equal to the minimum wavelength that need to be detected, but there are some ways to increase the measuring range but these techniques would limit the speed of the grating spectroscope [Lord57]. With FTIR spectroscopes the measured range is typically from 1000 cm^{-1} to 7000 cm^{-1}.

The setup of the new grating spectroscope will be described hereafter. First the general theory for gratings will be given. Then each element of the setup is discribed and typical values for the setup are given, like the resolving power, signal to noise ratio, and such.

3.1. General grating theory

Gratings are used to separate the different components of the spectrum. One particular type of grating is the so-called blazed grating, see figure 3.1. Here the grooves have a saw tooth profile and the facets of the grooves tend to reflect the light into the direction of the chosen

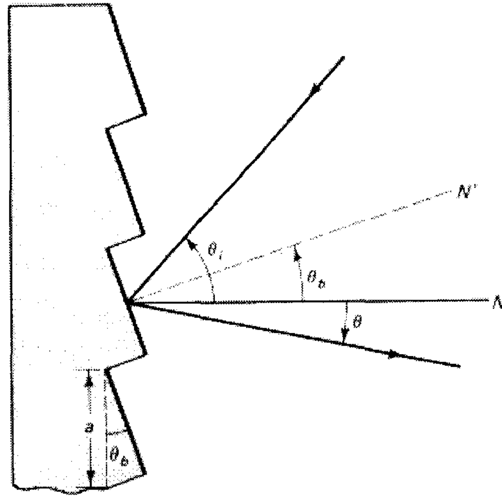

Figure 3.1: *Blazed grating and its relationship to various parameters associated with the grating.*

diffraction and therefore enhance the efficiency of the grating in that direction. Figure 3.1 also shows how some of the parameters associated with a blazed grating are defined. Here N is the normal of the grating plane, and N' is the normal of the groove face. The angle between the both normals is the so-called blaze angle θ_b. The light is incident on the grating at angle θ_i and it is diffracted at an arbitrary angle θ_m. Both angles are measured relative to the normal of the grating plane, and if they are on the same side of the normal N they have the same sign. The wavelength λ diffracted into that particular angular position θ_m can be calculated by the so-called grating equation:

$$a(\sin\theta_i + \sin\theta_m) = m\lambda, \tag{3.1}$$

where m is the order of diffraction and a is the size of each groove. It can be seen from equation 3.1 that overlapping of the different orders at the same angular position can occur i.e. at the same angular position a number of different wavelengths can exist. The non-overlapping wavelength range in a particular order is called the free spectral range F. If λ_1 is the lowest wavelength of the light incident on the grating then the free spectral range can be written as:

$$F = \frac{\lambda_1}{m}. \tag{3.2}$$

Two other important parameters for the grating are the dispersion D and the resolution R. The dispersion gives the angular separation per unit wavelength and is given by:

$$D = \frac{d\theta_m}{d\lambda} = m(a\cos\theta_i\frac{\partial\theta_i}{\partial\theta_m} + a\cos\theta_m)^{-1}. \tag{3.3}$$

The resolving power is a measure for the maximum obtainable *resolution* that can be achieved by a setup with a particular grating. The resolving power is the ability to produce distinct peaks for closely spaced wavelengths in a particular order and is given by:

$$R = \frac{\lambda}{(\Delta\lambda)_{\mathrm{min}}} = mN = \frac{W(\sin\theta_i + \sin\theta_m)}{\lambda}, \tag{3.4}$$

where N is the total number of the grooves on the grating, and W the total width of the grating perpendicular to the grooves. The last important parameter is the efficiency of the grating. Generally there are two types of efficiency associated with gratings. The *absolute* efficiency is the percentage of light diffracted into the required order compared to the incident light. The incident light off course has to have the right wavelengths to be diffracted. The *relative* or *groove* efficiency is the amount of energy diffracted in the right order compared with the energy that would have been reflected by a plane mirror of the same material. The latter type gives higher values for the efficiency. The efficiency of a grating is not easy to calculate. It depends for instance on the wavelengths, order, blazing angle, shape of the edges, polarization and the reflectance of the material. Therefore this information is in general given by the manufacturer of the grating. For a good grating in the infrared, the absolute efficiency can be more then 50% [Hurt92].

3.2. Optics setup

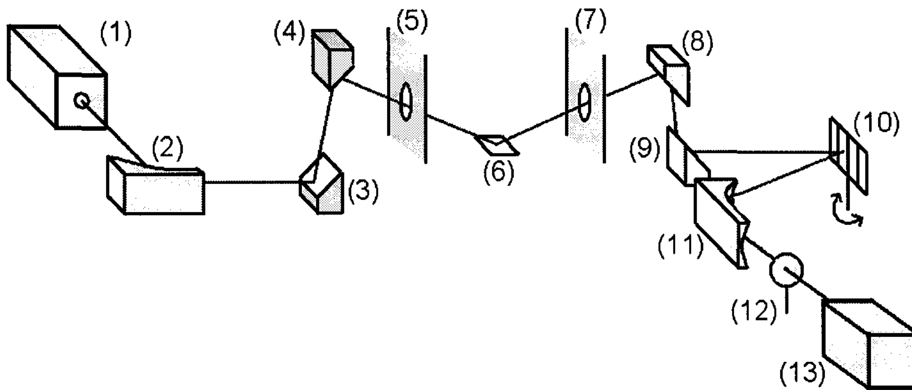

Figure 3.2: *The optical elements in the FGIR setup: (1) the cascaded arc as light source, (2) 90° off axis parabolic mirror (f=19 cm), (3) flat gold coated mirror, (4) 90° off axis parabolic mirror (f=36 cm), (5) KBr window in vessel, (6) substrate, (7) KBr window in vessel, (8) 90° off axis parabolic mirror (f=36 cm), (9) flat goldcoated mirror, (10) grating, (11) 90° off axis parabolic mirror (f=7.5 cm), (12) cut off filter, (13) MCT detector*

The optics of the setup used in the new Fast Grating InfraRed (FGIR) spectroscope are shown in figure 3.2. Each element in the setup will be described hereafter.

Cascaded arc

The cascaded arc (1) is used as a light source, because from previous experiments it was found out that it has a high intensity in the infrared higher then the 800 °C glowbar used in the FTIR spectroscope (Bruker Vector 22) [Hest98]. A description of the arc can be found for instance in the thesis of A.T.M. Wilbers [Wilb91]. The arc was operated in Argon, the Argon pressure was 1.8 bar, and the Argon flow was 10 ml/min. The current through the arc was set to 22 A. For the windows in the arc KBr crystal were used with a thickness of 4 mm. The radiating surface of the arc is $6*10^{-4}$ m^2 and the divergence of the beam exiting the arc is 75 mrad for the visible light.

The spectral distribution of the arc has been measured with the FTIR spectroscope. To do this the glowbar was removed from the FTIR. The light from the arc was then coupled into the FTIR at the same place where the glowbar used to reside with some mirrors. Also a cut off filter with the cut off at 7 μm was placed in front of the arc. This filter is the same as used in the FGIR setup. The transmission of the filter is given in figure 3.6. This filter was used to block light with higher wavenumber coming from the arc that interfered with the emission measurements. The result of the emission measurement is given in figure 3.3.

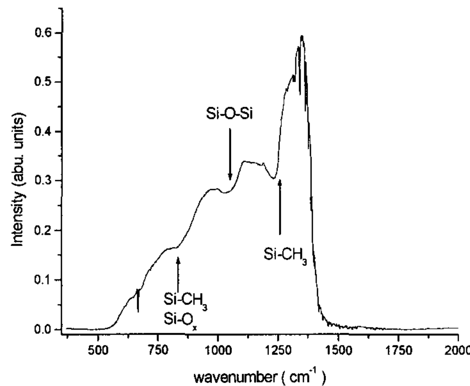

Figure 3.3: *Emission spectrum of the cascaded arc.*

Note the resemblance between figure 3.3 and figure 3.6. The emission of the arc without the filter in front would therefore be almost constant in the range of 700 cm^{-1} to 1300 cm^{-1}. Also drawn in figure 3.3 are the locations of the different absorption peaks that can be measured with the FGIR setup. It can be seen in figure 3.3 that the arc does not exhibit any large absorption or emission peaks in the desired wavelength range. Furthermore it can be seen that the filter is highly effective in blocking the light with a wavenumber above 1430 cm^{-1}. Finally it can be noted the intensity of the arc is highest near the cut off at 1300 cm^{-1} and it will drop to nearly zero at 500 cm^{-1} or 20 μm, this drop is primarily due to the cut off filter used.

If the light intensity from the arc is low, the light intensity of the arc can be increased by increasing the pressure inside the arc. To do this one a few changes need to be made on the arc, i.e. the windows in the arc need to be thicker. The pressure dependence of the light intensity of the arc has been measured for only a small pressure range. The current and gas flow through the arc were not changed. For these experiments the light emitted from the arc was focused on a MCT detector and the energy flux on the detector was measured. The cut off filter was placed between the arc and the detector, so only infrared light with a wavelength above 7 μm was detected. The results of the experiments are given in figure 3.4.

A pressure change of 15 % leads to a light intensity increase of 8 %. If the pressure dependence is linear and it is extrapolated to 5 bar, the light intensity would increase by 80 %. Similar experiments with a greater pressure range have been performed by M. van Hest [Hest98]. An increase in intensity of a factor 2 was found when increasing the pressure from 1500 to 4000 mbar. But this was measured at 2500 cm^{-1}.This increase in intensity was attributed to the higher electron density as well as the higher electron temperature for the plasma when the pressure in the arc is increased.

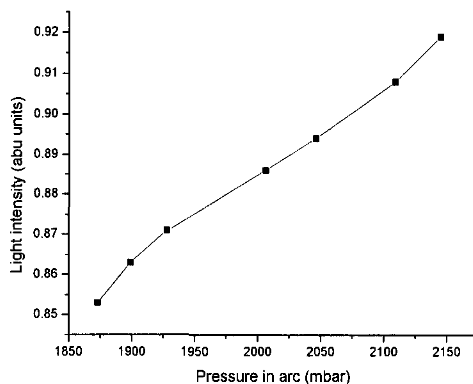

Figure 3.4: *The light intensity from the arc with the cut off filter in front as a function of the pressure in the arc.*

Focusing elements

The divergence of the light beam exciting the arc was measured and was found to be 75 mrad for the visible light. Because this divergence is too big for a setup with a total length of more then one meter, an 90° off axis parabolic mirror (2) is used to reduce this divergence. For the focal length 19 cm was chosen because from ray trace simulations it was found that this number gives good results in reducing the divergence. After the first 90° off axis parabolic mirror the beam is almost parallel and the divergence is less then 5 mrad.

Then the beam is transported and focused onto the sample (6) inside the vessel. This is done by two mirrors, one flat mirror (3) and 90° one off axis parabolic mirror (4) with a focal length of 36 cm. The sample can be substituted by an Attenuated Total Reflection (ATR) crystal but this makes no difference to behavior of the remaining part of the optical setup; The characteristics of the setup, like the sensitivity and signal to noise ratio, do change when using an ATR crystal. The description of the ATR crystal is given in chapter 3.5. For the windows (5) and (7) in the vessel KBr crystals are used, which has a high transmittance for infrared light. On the other side of the vessel there is an equivalent part of mirrors (8) and (9) so that the beam is again parallel. When this parallel beam hits the grating (10) it gets diffracted, and each wavelength is reflected into another angle. Each wavelength can now be seen as a separate parallel beam reflecting of the grating. A small wavelength band is then focused onto a MCT-detector (13) by a 7.5 cm focal length 90° off axis parabolic mirror (12). The other wavelengths will fail to reach the detector. The characteristics of the detector are described later.

Grating

The type of gratings defines the main part of the characteristics of the setup. For this setup a grating was chosen to measure absorptions of approximately 10 μm. To accomplish this a grating with a grating constant of 50 grooves/mm was selected, while this value would provide a good angular dispersion centered around 10 μm. The angular dispersion is high enough such that the light is diffracted sufficiently to be able to separate the different wavelengths in the incident light. Also is the angular dispersion small enough such that the rotational angles of the grating can be kept small, i.e. below 0.35 rad. When the angle of incident is zero rad and the off axis parabolic mirror is set such that the light diffracted at 1/6 π rad is focused

onto the detector it will measure light with a wavelength centered around 10 μm. If now the grating is rotated, different wavelengths will be focused onto the detector.

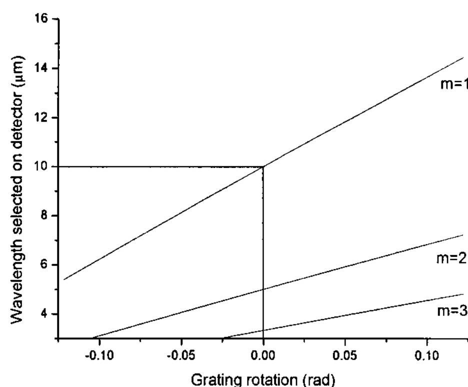

Figure 3.5: *wavelength of light that hits the grating as a function of the grating rotational angle. At zero degrees rotation, the angle of incident on the grating is zero, and the diffracted angle is 30 degrees and the grating constant is 50 lines/mm. m gives the order of the light diffracted.*

Figure 3.5 shows the wavelength range that hits the detector for light diffracted in the first three orders when the grating is rotated from -0.12 to 0.12 rad clockwise with respect to its initial position. It can be seen in figure 3.5 that the angular dispersion for the first order (m=1) at these low rotational angles can be approximated as being constant and is equal to 0.0268 rad/μm, and this value is obvious the same as if it was calculated by equation 3.3 with $\frac{\partial\theta_i}{\partial\theta_m} = 1$. Note that for the dispersion calculated by equation 3.3 a change in the mechanical angle $\Delta\theta_{grating}$ is the same as the change in the diffracted angle $\Delta\theta_m$, ($\Delta\theta_m = \Delta\theta_{grating}$).

Filter

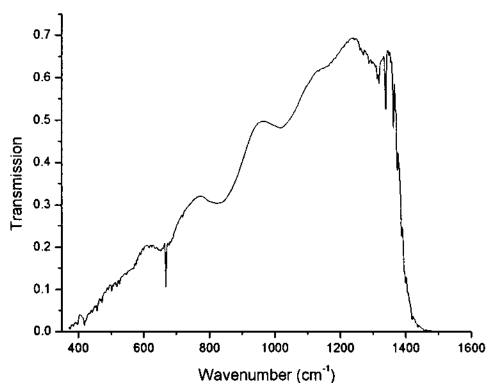

Figure 3.6: *Transmission spectrum of the cut off filter.*

Light from other orders will interfere with the desired signal as can be seen in figure 3.5. Therefore a cutoff filter (12) was introduced to the setup with a cut off near 7 μm / 1420 cm^{-1}. The transmission of this filter is given by figure 3.6. This filter has a sharp cut-off and the transmission for wavelengths below 7 μm is small or zero. Furthermore the filter will not

reduce the light intensity in the desired wavelength range by more then 50%. The free spectral range can now be calculated by equation 3.2 and is 7 μm. The setup can measure absorption peaks in the range of 7 μm to 14 μm, and the grating needs only to rotate 0.19 rad to scan this wavelength range.

3.3. Mechanical and electronical setup

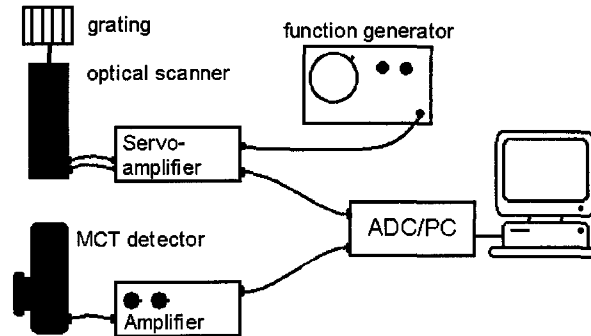

Figure 3.7: *The mechanical and electronical parts of the setup.*

Optical scanner

The signal and electronical setup is given in figure 3.7. The optical scanner, model 6650, on which the grating is mounted, is controlled by the servo-amplifier, Micromax series 670. The optical scanner and the servo amplifier are both manufactured by Cambrigde Technology Incorporated. The load on the optical scanner must be between 0.45 gm-cm^2 and 90 gm-cm^2. The basic operation of the servo is: Accept a command input voltage signal and turn it into a stable, repeatable, angular position of the scanners output shaft. The amplifier does this by combining the input information with the feedback information from the scanner (the position and speed of the scanner) to form an error signal. The servo then strives to force this signal to zero by rotating the scanner's shaft. It is this following of the input signal that allows it to control the scanners angular position. The grating will rotate 34.9 mrad per 1 volt (2 degree per 1 volt) applied on the input of the servo amplifier. The input range of the servo-amplifier is -10 V to 10 V.

The input signal for the servo-amplifier is generated by a HP function generator. A sinusoidal signal was chosen because this would lead to the highest frequency the rotation of the grating could be driven by. The maximum frequency of the applied signal at which the optical scanner will work properly depends also on the applied amplitude. For large frequencies (300 Hz) only small amplitudes can be set. Otherwise the scanner cannot follow the input signal and the grating will start to stutter. The maximum amplitude the grating can be driven by the scanner as a function for each frequency is given in figure 3.8.

While the grating needs to rotate a total of 0.19 rad, the maximum amplitude of oscillation only needs to be 0.095 rad. From figure 3.8 it shows that the scanner is then able to perform this oscillation with a frequency up to 180 Hz. The maximum oscillating frequency of the grating will also be the main limiting factor for the time to measure one full spectrum.

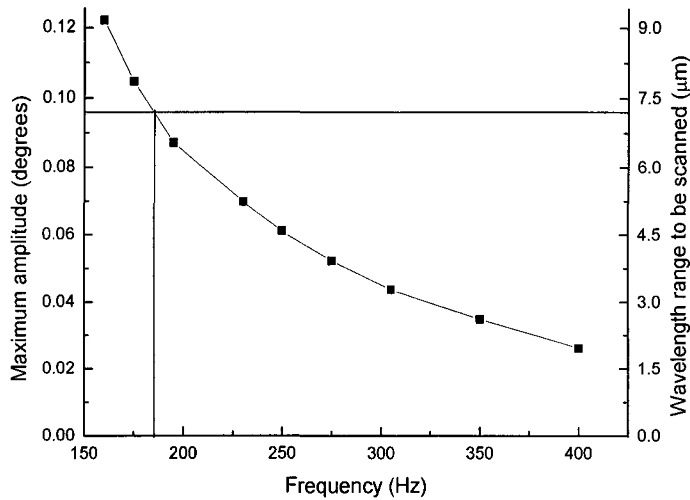

Figure 3.8: *The maximum amplitude for the oscillation and the wavelength range scanned as a function of the oscillation frequency of the optical scanner with the used grating.*

The servo-amplifier also gives the current angular position of the grating with an accuracy of 1.5 μrad. The scale for the output signal is the same as for the input signal: 28.6 V per rad (0.5 volt per degree).

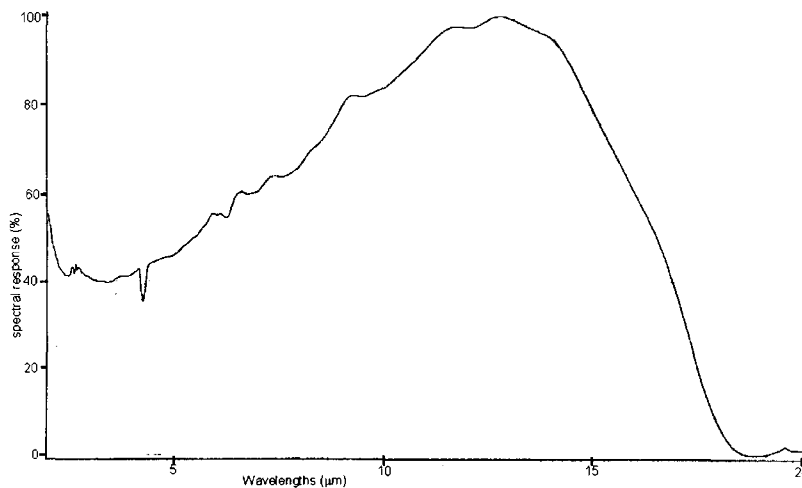

Figure 3.9: *The detector efficiency for each wavelength.*

Detector

The light is detected by a liquid Nitrogen cooled MCT detector. Here the model D316/6 from InfraRed Associates, Inc. has been used. The active area of the detector is 1 mm^2 and the field of view is 60 degree. The efficiency of the detector is given in figure 3.9. It can be seen from figure 3.9 that in the desired range of 7 to 14 μm the efficiency is always above 60% and the efficiency has a maximum of almost 100% at 13 μm. The efficiency measurements were performed by the manufacturer. Because the responsivity of the detector was low, a custom

made amplifier was made to exchanged the standard amplification circuit on the detector. The old amplifier consisted of two steps. First a DC signal from the detector was amplified, and in the second step the DC signal was converted to a AC signal. The new circuit is the first step is almost the same, except that the amplification and the offset of the DC signal are now tunable. The second amplification step was left out, so the new amplifier is DC and the old was AC. The response time of the detector is 5 μs.

ADC/PC

When measuring a spectrum the function generator is switched on and the grating starts to oscillate. An ADC constantly samples the signal from the amplifier of the detector and the angular position of the grating on the servo-amplifier. The ADC used is a National Instrument, type 6035E, which is capable of measuring with a sample frequency of 200 kHz and has a resolution of 16 bits. The measured intensity spectra are then stored on a computer where they can be further processed. For the measurement and analysis of the data a new program has been written in Measurement Studio 6.0/Labwindows/CVI 5.5.

3.4. Resolving power / Timescales

As stated before the measuring time for only one spectrum must be of the order of 10 ms or less. Each period of the grating two spectra can be measured; one when the grating is moving clockwise and one when the grating is moving counter clockwise. For a grating frequency of 175 Hz, the measuring time is for one spectrum is 2.9 ms. During this time the ADC can sample both channels together with 200 kHz. The number of data points measured for each spectrum N can be calculated by the following equation:

$$N = \frac{1}{2f_{oscillation}} \frac{f_{sample}}{N_{channels}}, \tag{3.5}$$

where f_{sample} is the sample frequency of the ADC, $N_{channels}$ the number of channels to be measured, and $f_{oscillation}$ the frequency the gratings oscillates with. In this case each spectrum would consist of 285 (position, intensity)-data points.

Resolving power

The resolving power is the ability to resolve closely located peaks and is defined as the ratio between the smallest change in wavelengths it can resolve and the wavelength it operates on. The resolving power can be calculated by equation 3.4, but this equation was derived for a spectrograph with a perfect focus. In that case the resolving power is limited by the width of a monochromatic line. But here the resolving power of the setup is mainly determined by the focusing of the light diffracted of the grating onto the detector, although other effects will also play a role. To get an idea about the resolving power of the setup, a simple model was used, see figure 3.10.

The 90° off axis parabolic mirror is modeled as a plain lens. At the grating light is diffracted in all angles and from all places y on the grating. A lens is placed a distance of L_1 from the grating. The lens with a focal length of f is placed in such a way that all the light diffracted in one particular angle θ_0 is focused in the focal point. At this point the detector is placed. Because the detector is not infidesimal small but has a active area of d^2 also light with a slightly different angles θ will be detected. This will lead to the reduction of the resolving

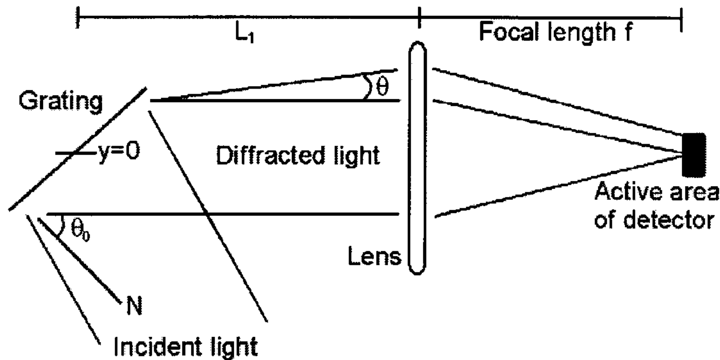

Figure 3.10: *Schematic representation of the model to calculate the resolving power of the setup, with the definition of the various parameters used in the model..*

power of the setup. The light from the grating that hits the detector can be calculated with the so-called matrix method [Pedr93]:

$$\begin{bmatrix} y_1 \\ \theta_1 \end{bmatrix}_{\text{detector}} = \begin{bmatrix} 1 & f \\ 0 & 1 \end{bmatrix} \begin{bmatrix} 1 & 0 \\ -\frac{1}{f} & 1 \end{bmatrix} \begin{bmatrix} 1 & L_1 \\ 0 & 1 \end{bmatrix} \begin{bmatrix} y \\ \theta \end{bmatrix} \tag{3.6}$$

$$\begin{bmatrix} y_1 \\ \theta_1 \end{bmatrix}_{\text{detector}} = \begin{bmatrix} f\theta \\ -\frac{1}{f}(y + \theta L_1) + \theta \end{bmatrix} \tag{3.7}$$

Note that the angles used in this method are in radial convention. The top part of equation 3.7 gives us which light (y,θ) which reaches the detector. For y_1, half the height of the active area (1x1 mm^2) of the detector is chosen and the focal length of the 90° off axis parabolic mirror which is 75 mm. Now light that is diffracted with an angle of $\theta_0 - 6.7$ to $\theta_0 + 6.7$ mrad will also reach the detector.

The bottom part of equation 3.7 gives the angle of incident onto the detector for each θ. The field of view for the detector is 60 degrees. For any reasonable values for each parameter (y=1.5 cm, $L_1 \lesssim 2f$) θ_1 is smaller then the field of view of the detector and all the light that reaches the detector will also be counted.

When the dispersion is given, the resolving power can be calculated. The dispersion can be calculated by equation 3.3, but because the incident angle is not changed in this model, $\frac{\partial \theta_i}{\partial \theta_m}$ is equal to zero. The dispersion is then approximately 0.0577 rad/μm, and the wavelength interval on the detector is then 0.23 μm. If the grating was placed to measure 10 μm light also light with a wavelength from 9.89 μm to 10.12 μm would reach the detector. The resolving power can now be calculated and is for the FGIR at 10 μm 43. The upper theoretical limit for the resolving power is given by equation 3.4 and is 1000.

An absolute minimum condition for the resolving power is that it can resolve two different absorption peaks in a spectrum. The 1260 cm^{-1} and the 1090 cm^{-1} peak are closest together in a typical spectrum, and to be able to resolve them, the resolving power must be at least 10. A better condition for the minimum resolving power is that the absorption peak widths are not increased by more then a factor of two with the FGIR setup. A typical full width half maximum for the Si-CH_3 at 1260 cm^{-1} is 30 cm^{-1}. This would then lead to a minimum resolving power of 42, and this condition is just met.

A way to increase the resolving power of the FGIR setup is to place a slit in front of the detector, so the wavelength band that reaches the detector will be smaller. Another way to

increase the resolving power is to use deconvolution on the measured spectra. To measure a spectrum from 7 μm to 14 μm with a resolving power of 43 only 31 data points need to be measured. With the FGIR setup it is possible to measure more datapoints, at 175 Hz 285 data points are measured per spectrum. This excess in data points can be used to deconvolute the spectrum. Theoretically a spectrum with a resolving power of 200 could be obtained with the FGIR setup after deconvolution. But there are a few problems with deconvolution: noise on the spectra will generate more noise in the deconvoluted spectra. Also the apparatus profile of the FGIR setup needs to be exactly known for a such a deconvolution [Jans96].

The resolving power will drop when the beam that hits the grating is not parallel but divergent. If the beam has a difference of 5 mrad, which is not very unlikely, then the resolving power would drop to 25. There are two main problems with aligning the setup to get a parallel beam. First is that the 90° off axis parabolic mirrors need to be placed very precise. Small misalignments in the mirrors can lead to serious errors with the focusing [Heme01]. The angle between the incident and reflected beam must be very close to 90 degrees. Also the light beam must hit the mirrors in the center.

The other problem is with the 36 focal length off axis mirrors used in the FGIR setup. The focal length is a bit to short to get the focus onto the substrate in the vessel. The distance between the substrate and the vessel wall is a bit more then 36 cm. This also leads to some problems with creating a parallel beam for the grating. If mirrors with another focal length are used this problem will seize to be. However such mirrors are not commercially available.

Resolution

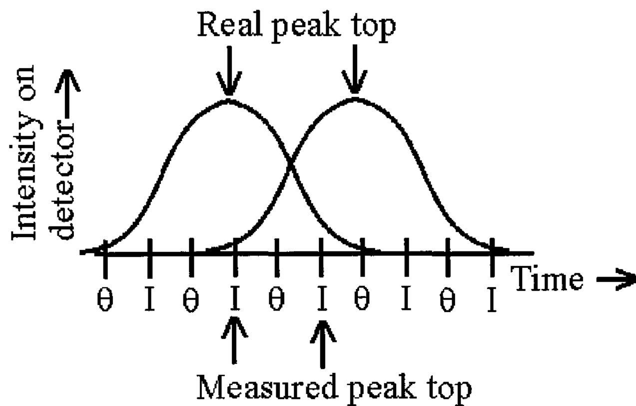

Figure 3.11: *Two different monochromatic peaks and their minimal difference that can be detected. θ and I give the time where or the angular position of the grating θ or the intensity on the detector I gets measured.*

The resolution is the smallest change of wavelength that the setup is able to detect. The resolution must be below 0.1 μm or the identification of the absorption peaks can become a problem. The angular position of the grating and the intensity on the grating are read sequential after each other. The resolution is mainly determined by the time between to different angular position measurements. The error in the angular position of an intensity peak can be estimated as two times the change in angular position between two sequential angular position measurements as can be seen in figure 3.11. The resolution $\Re$ can now be calculated by:

$$\Re = 8\pi \frac{f_{grating}}{f_{sample-rate}} \frac{A}{D}, \quad (3.8)$$

where $f_{grating}$, $f_{sample-rate}$, A, and D are the frequency of the grating oscillation, the sample frequency of the ADC, the maximum amplitude of oscillation, and the dispersion, respectively. If the grating frequency was set to 175 Hz, the sample rate at 200 kSamples/s, the maximum oscillation at 5.5 degrees and the dispersion was taken 0.0276 rad, then the resolution would be 0.08 μm.(or 8 cm^{-1} at 1000 cm^{-1}).

3.5. Signal to noise ratio

What would now be the signal to noise (S/N) ratio of the measured spectra with this setup? To answer this question the emission of the light source needs to be know, the transmission of the system and the detection efficiency.

To make the calculations easier, the calculations of the transmission are performed at a constant angle of the grating when the signal on the detector is highest. This is when the detected wavelength is close to the cut-off edge of the cutoff filter. At the end of the calculation a generalization for the S/N ratio for the rest of the spectrum is made.

The light source (cascaded arc) was modeled as a blackbody radiator with a temperature T of 12000 K and an emissivity of 20% [Ragh01]. The number of photons emitted per second per solid angle of a blackbody radiator as a function of the wavelength $N(\lambda)$ [s^{-1}sr^{-1}]is given by:

$$N(\lambda) = \frac{c}{\lambda^4} \frac{1}{\exp(hc/\lambda kT) - 1}, \quad (3.9)$$

with c the speed of light, h the Planck constant, and k the Boltzmann factor. The radiating surface of the arc is 6*10^{-4} m^2 and the solid angle is 0.012 sr. When the grating is not moving still a small bandwidth of light is incident on the detector, see section 3.4. This bandwidth was calculated and found to be approximately 0.23 μm. Assume that the detector is placed such that the wavelengths between 7.1 μm and 7.33 μm are focused onto the MCT detector. Then integrating expression 3.9 over the appropriated wavelength range gives that the arc generates about 2.0*10^{17} photons within these wavelength band. The transmission of the system was calculated in two steps. The first is the calculation involves the losses in the optical system due to the various *diaphragms* in the system. The diaphragms in the system are the vessel windows and the finite sizes of the various optical elements in the system. For this step a ray trace program program was used, called interactive ray trace (IRT). This program is made by Parsec Technology Inc. The second step gives all the reflection and transmission losses in the system, and then the total transmission of the system can be calculated.

IRT

An Interactive Ray Trace (IRT) simulation of the optical setup has been performed to check the geometrical losses (focusing and diaphragm losses). Figure 3.12 show the setup model used; table 3.1 describes each element in the model. In the simulation the use of an ATR crystal as well as a substrate is taken into account. The off axis parabolic mirrors were modeled as plain lenses and their reflection/absorption coefficients were not taken into account. The flat mirrors were also not taken into account. Because with the cascaded arc the light is generated

Table 3.1: The parameters used in the simulation

element number	element name	type	distance to previous element	size of element
1	Cascaded arc	Lightsource/diafragm	-	-
2	Off axis parabolic mirror	Lens f=190 mm	140 mm	15x15 mm^2
3	Off axis parabolic mirror	Lens f=360 mm	200 mm	15x15 mm^2
4	Window	Diafragm	50 mm	49 π mm^2
5	ATR crystal/ Substrate	Diafragm / None	300 mm	10x0.6 mm^2
6	Window	Diafragm	300 mm	49 π mm^2
7	Off axis parabolic mirror	Lens f=360 mm	50 mm	15x15 mm^2
8	Grating	None	250 mm	-
9	Off axis parabolic mirror	Lens f=75 mm	250 mm	15x15 mm^2
10	Detector	Diafragm	70 mm	1x1 mm^2

throughout the whole arc channel, the arc was modeled as 20 light sources on a straight line. The divergence of the arc was set to 75 mrad.

From the simulation it was concluded that when a substrate was used, the transmission would be 70%. The main losses are on the first window (15%) and on the detector (10%). When an ATR crystal is used in the setup the transmission drops to 10%. The main loss is on the ATR crystal. Figure 3.13 show the spot size on the ATR crystal. The spot is approximately 6 mm in diameter, and the entrance of the ATR crystal is 20 mm width and 0.6 mm high. Therefore approximately 80% of the light incident on the ATR crystal misses the ATR entrance and is lossed as can be seen in figure 3.13. In the case of an ATR 15% of the light incident on the detector is not focused onto the detector as can be seen in figure 3.13. Another important parameter for the setup is the divergence of the beam onto the grating. This parameter influences the resolving power of the setup. Without the ATR crystal the divergence was found to be 4 mrad. With the ATR crystal the divergence reduces to 1 mrad, because the ATR works as a collimator. The setup is sensitive for misalignment. When, for instance, the first 36 cm focal length 90° off axis parabolic mirror is moved back or forth 10 mm, an increase in divergence of 5 mrad is easily obtained.

Reflection and transmission losses

In the above IRT simulation only the geometrical losses are calculated. But there is also light loss due to non-perfect reflection and transmission for the optical elements. There are two aluminum and four gold coated mirrors in the setup, furthermore there are two KBr-windows,

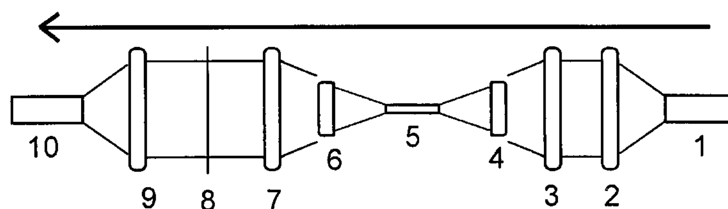

Figure 3.12: *The optical elements used in the IRT simulation as given in table 3.1.*

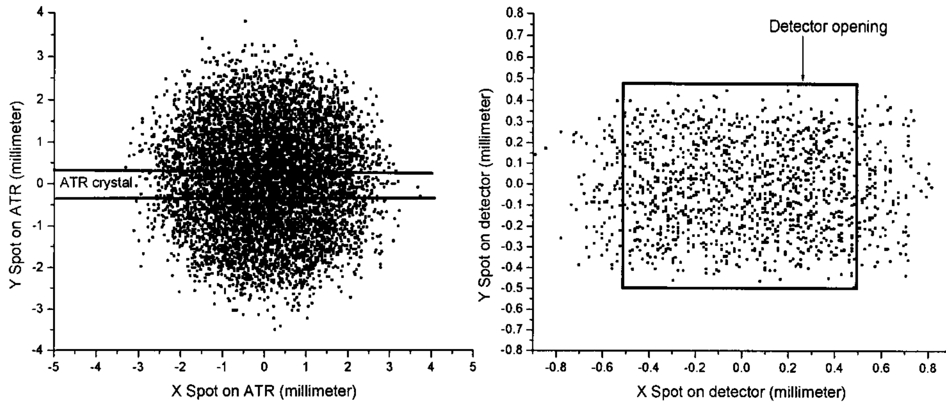

Figure 3.13: On the left *the spot incident on the ATR crystal. The lines give the size of the entrance of the ATR crystal. On the right the spot on the detector.*

Table 3.2: The assumed reflection and transmission coefficients for the various elements in the FGIR setup.

Element	Transmission or reflection coefficient
Gold coated mirror	98 % reflection
Aluminum mirror	70 % reflection
KBr window	80 % transmission
Grating	70 % reflection and 30 % in the right order
Filter	70 %
Substrate	70 % reflection
ZnSe ATR crystal	70 % transmission [Bruk97]

one grating and one cut off filter. Also are there losses on the substrate or ATR crystal.

Table 3.2 gives the assumed reflection and transmission coefficients for the various elements in the FGIR setup. The grating however cannot be described by only one reflection coefficient. The grating is made from Aluminum. The reflection coefficient is near 70 %, but light is also diffracted into the first order but also in other orders. The relative efficiency is at least 30 % [Hurt92].

The total transmission and reflection losses come then to a total of 96.8 %. Together with the transmission of the setup calculated in the IRT simulation, the total transmission of the FGIR setup is with a substrate 2.2 % and with an ATR crystal 0.31 %.

Detector

The number of photons that enter the system is 2.0 $*10^{17}$, and the transmission of the system is 2.2 % with a substrate. Therefore 4.4 $*$ 10^{15} photons reach the detector every second. The detector has a efficiency of 60% for photons with a wavelength of 7.2 μm. Each detected photon has an energy of about $2.75*10^{-20}$ J and then the energy flux detected by the detector is then $7.3*10^{-5}$ W. With a responsity of the detector of 1500 V/W this would lead to a signal of 100 mV, which is easily detected.

The noises in the setup are more difficult to calculate. The main noises are the fluctuations of the light intensity of the arc, the mechanical vibrations in the setup, and noises in the amplifier of detector. The noises include 1/f noise, g-r noise (generation-recombination noise)

by recombination of electron and hole, and Johnson noise as a thermal noise. Also noise from the background must be included. The noises in the detector with the old amplifier are given by the manufacturer and were 3 mV and is noise was largely independent of the light intensity on the detector. With the old amplifier the signal to noise ration would be 33, which would make the setup able to detect 3% absorptions.

To increase the signal to noise ratio a new amplifier was build, but with the new amplifier the responsivity of the detector has become unknown. It is believed that the responsivity increased by at least a factor of 8. To measure the signal to noise ratio of the FGIR setup, the setup was build around the depo 1 setup, the same way it is going to be used to monitor deposition. As a substrate a Silicon substrate was used. Then various intensity spectra were measured while nothing changed in the setup. These spectra should therefore all be the same. If then the intensity spectra are divided by the first intensity measured the S/N can extracted. Figure 3.14 shows on the left the measured intensity spectra and on the right the divided light spectra.

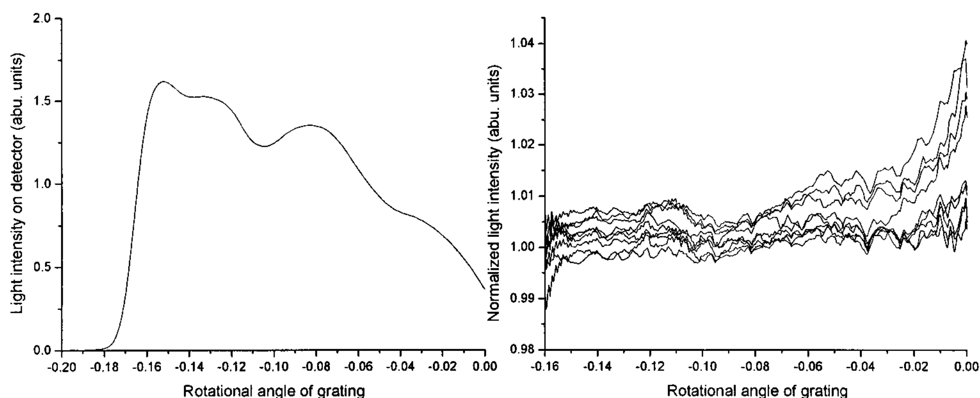

Figure 3.14: *Left: Light intensity on the detector as function of the rotation angle. Right: Changes in the measured light intensity between different intensity spectra.*

In figure 3.14 can be seen that the change in light intensity is at most 1% at most rotational angles. Only when the light intensity on the detector is low, for rotational angle between -0.04 rad and 0 rad, the changes in light intensity become bigger. If all the changes in light intensity are all contributed to noise then the signal to noise ratio can be calculated from 3.14 and is 100, for most of the spectrum, but when the light intensity on the detector becomes smaller the signal to noise ratio drops to 25. With the new amplifier absorptions of 1% can be observed. It seems that the noises in the spectra are mainly independent of the light intensity on the detector. The signal to noise ratio is then mainly a function of the signal, i.e. light intensity on the detector. Then the signal to noise ratio S/N can be calculated with:

$$\left(\frac{S}{N}\right) = \frac{S}{S_{best}}\left(\frac{S}{N}\right)_{best}, \tag{3.10}$$

For thin films the signal to noise ratio of 1% can be too small to measure the absorption peaks of the film. There are a few ways to improve the sensitivity of the setup for small absorptions. For instance the signal, i.e. the light intensity on the detector, can be increased by increasing the pressure in the cascaded arc. The increase in pressure would lead to a higher light intensity from the arc, and more light would be detected.

ATR

Another way to increase the sensitivity for small absorptions of the FGIR setup is the use of an ATR (Attenuated total reflection) crystal as substrate. With this crystal the absorptions are enhanced and become easier to detect. Figure 3.15 show the principal of an ATR crystal.

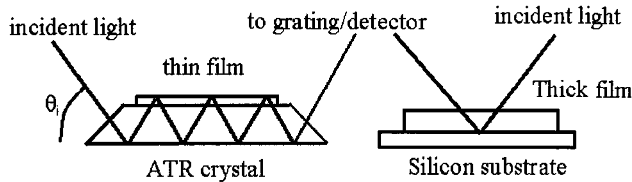

Figure 3.15: *The principle of an ATR crystal versus a Silicon substrate.*

Instead of a single reflection on the surface of the substrate the light is focused on the entrance of the ATR crystal. Because the ATR crystal has a high refractive index, the light is trapped in the crystal, due to total internal reflection and starts moving through the crystal. At each reflection on the top the beam also goes through the film on top of the ATR crystal. This way the path length of the light traveling though the film of interest is increased. The number of reflections N on the top plane of the ATR crystal can be obtained by:

$$N = \frac{l \tan \theta_i}{2t}, \tag{3.11}$$

where t is the length of the ATR crystal and θ_i the angle of incident. For thin films, i.e. the absorptions are less then 1% or 2% in single reflection, the number of reflections is equal to the increase in the absorption. For thick films the attuated wave theory must be used , and effects as depth of penetration, electric field strength, sampling area and index matching need to be considered to explain the absorptions [Harr67].

The ATR used in the setup is a ZnSe crystal with an refractive index of 2.4. The length of the crystal is 5 cm and it is 0.5 mm high. The angle of incident is about 0.6 rad. Then the number of top reflections is 35. The absorptions would be 35 times bigger then they would be in single reflection with the same film. The tradeoff with ATR is that the signal intensity drops. For the FGIR setup the signal will be 7 times lower with an ATR compared to a substrate. The Signal to Noise ratio of the setup with an ATR crystal was also measured on the same way as with a Silicon substrate and found to be 33. This is mainly due to the smaller light intensity on the detector when an ATR is used, however the noises are somewhat decreased.

3.6. Summary

Various parameters for the setup has been calculated, and these are shown in table 3.3. For the sensitivity of the ATR two values are given. The first is the absolute absorption intensities that can be measured. The second value gives the value of the absorption if the same film thickness was deposited on a Silicon substrate, and the absorption was measured in single reflection. If any changes to the FGIR setup are made some values in table 3.3 should be recalculated. For instance another grating can be placed on the optical scanner to measure different absorption peaks. This would also affect the other optical elements in the setup. If the grating is changed also another cut off filter has to be used.

Table 3.3: The various parameters associated with the FGIR setup

Parameter	Value
Measuring range	7 μm to 14 μm
Resolving power	40
Resolution	0.08 μm
Measuring time	> 2.9 ms
Signal to Noise (substrate)	100
Sensitivity	1 %
Signal to Noise (ATR)	33
Sensivity (ATR/substrate)	3 % / 0.08 %

4. Results and Discussion

4.1. Post deposition treatment

4.1.1. General introduction to the results

Plasma assisted CVD deposition of SiO_2 films with the cascaded arc can be a valuable substitute for other SiO_2 deposition methods for certain applications of the films. The strength of the method is mainly its high deposition rate, this can be up to 300 nm/s [Mitu99]. The main problem is the high Carbon/Hydrogen concentration in the film. For that reason the films are qualified as SiO_2-like or $SiO_xC_yH_z$ instead of SiO_2. One possible way to decrease the carbon concentration in the films is to use a post deposition treatment on the films. After the deposition the films are exposed to an Argon/Oxygen plasma. It is then assumed that the Oxygen atoms diffuse into the SiO_2-like layer and react with the Carbon in the film and volatile species are created. The volatile species are then removed from the film.

In this chapter the results and the discussion of the post plasma treatment experiments are given. For the experiments the depo 1 setup has been used. A description about the experiment and the steps involving the experiment can be found also in section 2.3. The films on which the treatments were performed on were all deposited with the same process parameters, and the composition and thickness of the deposited films are all similar. For the substrate for the films (1,1,1) Silicon wafers were used.

Two distinct series for the treatment process parameters have been measured. The first series varies the time of the post deposition treatment. This could give information about the rate in which the reactions occur in the film and the type of transport of the reacting particle in the film. For three different oxygen flows the changes in the films were monitored as a function of treatment time. For each treatment time a new sample was prepared and a new deposition was performed. Then the film was exposed to the post treatment plasma. No sample was plasma treated more then once. The plasma process parameters for this series are given in table 4.1.

The other series investigates the effects of the Argon/Oxygen mixture of the plasma during the post deposition treatment on the SiO_2-like films. For these experiment the Oxygen flow through the nozzle of the arc was varied, while the other process parameters were held constant. The process parameters used are given in table 4.2.

Table 4.1: The process parameters used for the post treatment in the time series.

Parameter	Value
Argon flow through arc	100 sccs
Oxygen flow (injected at nozzle)	1, 5, or 17 sccs
Current through arc	75 A
Temperature substrate	50 °C
Post treatment time	0.5, 1, 2, 5, 15, 30, and 60 minutes

Table 4.2: The process parameters used for the post treatment in the oxygen flow series.

Post plasma treatment parameters	Values
Substrate temperature	50 $°C$
oxygen flow	0, 1, 2, 3, 4, 5, 6, 8, 10, 12, 14, and 17 sccs
argon flow	100 sccs
current through arc	75 A
treatment time	15 minutes

A typical treatment

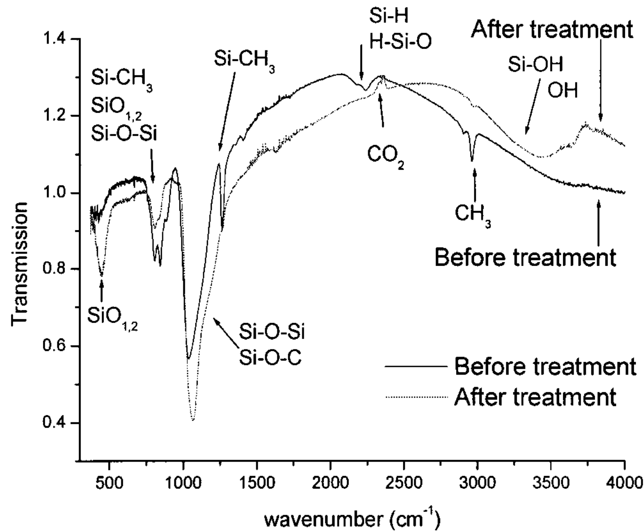

Figure 4.1: *Typical transmission spectra before and after treatment.*

Before and after treatment the films were measured *ex-situ* with FTIR spectroscopy and the changes in the amount of various bonds in the SiO_x-like material were measured. Figure 4.1 shows the transmission spectra of the SiO_2-like layer before and after a typical post deposition treatment. Table 4.3 shows the typical absorption peaks found for a SiO_x-like film deposited with HMDSO. The following peaks have been used in the analysis of the films: The CH_3 stretching absorption peak at 2960 cm^{-1}, and the Si-CH_3 vibration absorption peak at 1260 cm^{-1} were measured to monitor the amount of methyl bonds in the film, and this is an indication for the total Carbon concentration in the film. The Si-OH and OH absorption peaks at 3000 to 3600 cm^{-1}, and the $SiO_{1,2}$ at 450 cm^{-1} were measured to see if Oxygen is built into the layer. Finally the Si-H and H-Si-O peaks at 2250 cm^{-1} were used to determine the Si-H bonds in the material.

The Si-O-Si absorption peak at 1070 cm^{-1} has not been included while it overlaps with the Si-O-C absorption peak. Also the absorption peaks in the absorption band between 800 cm^{-1} and 850 cm^{-1} have been ignored due to this overlap.

In figure 4.1 it is shown that the post deposition treatment gives an decrease in the methyl related peaks Si-CH_3 and CH_3 as expected. Also a decrease in the Si-H peak can be noted. Furthermore the Oxygen related peaks, Si-$O_{1,2}$ and Si-OH are increased. To see how the absorption peaks changed in time the treatment times have been varied and its effects on

Table 4.3: The various absorption peaks in the spectra

Bond type	Location absorption peak	Reference
Si-H	2300-2100 cm^{-1}	[Kash91]
Si-OH / OH	3000-3600 cm^{-1}	[Naka84]
$Si-CH_3$	1260 cm^{-1}	[Kash91]
CH_3	2960 cm^{-1}	[Kash91]
Si-O-Si	1090-1020 cm^{-1}	[Kash91]
Si-O-C	1090-1020 cm^{-1}	[Kash91]
Si-O	430-450 cm^{-1}	[Naka84]
$Si-O_2$	430-450 cm^{-1}	[Naka84]

the changes of the absorption have been measured. The absorption peaks can be quantized in two ways: the absorption peak area and the maximum intensity of the absorption can be calculated. The methods for both calculations can be found in section 2.3.

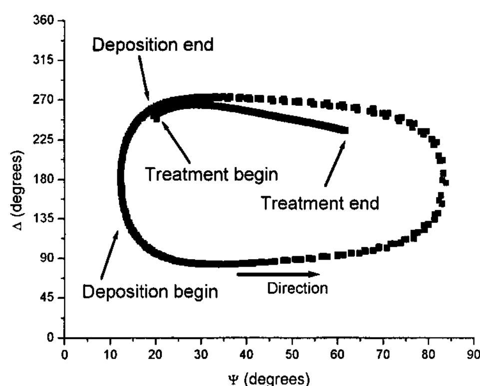

Figure 4.2: *A typical measured* $\Psi - \Delta$ *trajectory during the deposition and during the post treatment.*

During the treatment as well as the deposition the samples were monitored by means of ellipsometry. Figure 4.2 shows a typical measured $\Psi - \Delta$ trajectory during the deposition and the post deposition treatment. From the ellipsometry measurement the thickness and refractive index can be calculated. The SiO_x-like film deposition can be modeled as one growing layer with a constant refractive index. Because the refractive index is an indication for the Carbon content in the deposited film, it can be concluded from the ellipsometry measurements that the film grows homogeneously and the Carbon is distributed evenly inside the film [Mitu99]. The $\Psi - \Delta$ trajectory during the post deposition treatments were not simulated. If no extra knowledge about the layer during treatment is available, the simulation of the spectrum has a large degree of freedom, and the simulation becomes a mathematical exercise with no physical relevance. The optical thickness obtained by the FTIR spectroscope does not have this problem. The way to obtain the optical thickness from the transmission spectrum from the FTIR spectroscope can be found in section 2.2. The optical thickness obtained by this method can be compared with the optical thickness obtained with ellipsometry after the deposition has been performed. The differences in the optical thickness obtained with the two different methods are at most 20 nm.

4.1.2. Film properties versus time

The measurements were performed to find the characteristic times for the processes in the film during the post treatment. It shows how the film alters as a function of time. From these experiments the transport mechanism for the Oxygen through the film can be identified. Also it can be seen if and when the changes in the SiO_x-like would stop when the treatments of the films prolonges. The experiments were performed as was descibed in section 2.3. The results of the experiments are described here.

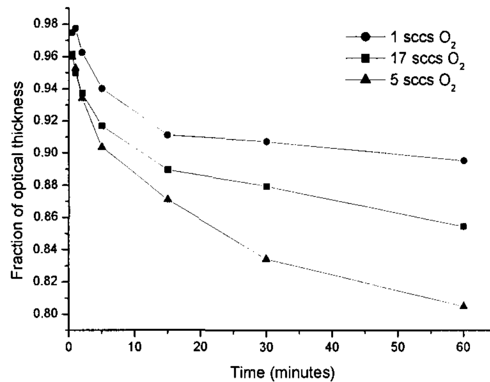

Figure 4.3: *The fraction left of the optical thickness after the plasma treatment as a function of the time.*

The first parameter investigated was the optical thickness of the layer. The refractive index of the SiO_2-like films is higher when there is a high Carbon concentration in the film [Mitu99]. Also the thickness of the film can decrease when Carbon is removed from the film. Therefore when the carbon concentration drops in the film also the optical thickness will drop. The optical thickness of SiO_2-like film was measured before and after the post treatment with the FTIR spectroscope, and the fraction of the optical thickness after treatment compared to the optical thickness before treatment was calculated.

Figure 4.3 shows the fraction left of the optical thickness after the post treatment versus the treatment time. It can be seen that the change in the optical thickness seems to decay exponentially in time. In the beginning the changes are fast and then they slow down. At the beginning the methyl groups are throughout the whole SiO_2-like layer, and in the beginning the methyl groups on the surface are broken. After a while the methyl bonds at the surface are broken down and the oxygen now needs to diffuse through the layer to find other methyl groups where it can react with. This will slow down the methyl removal process in time. To obtain a significant change in a SiO_2-like layer of 0.5 μm, the treatment must be at least one minute, but then only the top part of the layer is then changed.

The films treated with the low oxygen flow through the nozzle of the arc show the least change. The films treated with intermediate oxygen flow, 5 sccs, shows the largest change in the optical thickness and the film treated with 17 sccs oxygen flow is in between. This effect can be noted for most of the parameters that characterize the film and this effect is investigated in more detail in section 4.1.3.

A more direct way to measure the Carbon content in the film is to measure the absorption peak area of the Si-CH_3 (1260 cm^{-1}) and the CH_3 (cm^{-1}) absorption peaks. Before and after the treatment the peak area was measured and the fraction left of the peak area after treatment was calculated. Figure 4.4 shows both methyl related absorption peaks as a function of time

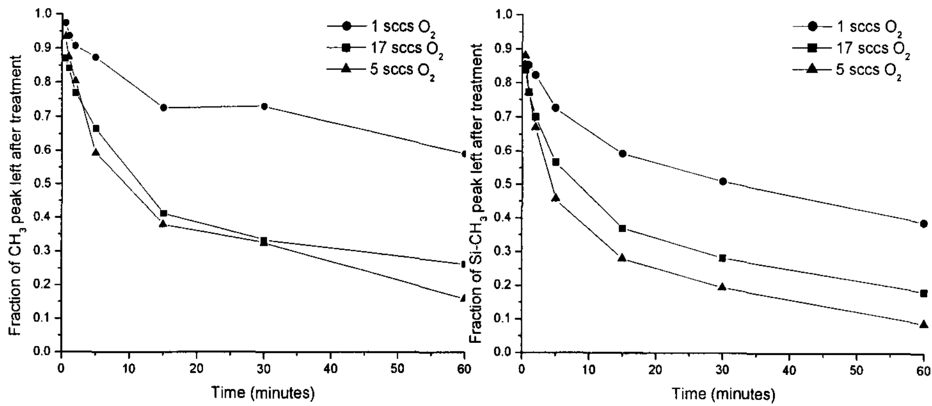

Figure 4.4: *The fraction left of the CH_3 (left) and the Si-CH_3 (right) absorption peaks after treatment as a function of treatment time.*

and for different oxygen flows for the post treatment. It can be noted that the longer the treatment time the more CH_3 bonds are broken, but the rate of this process will drop in time. This results in the seemingly exponential decay of the methyl measured, although the graph cannot be fitted by an exponential decay function.

In figure 4.4 the Si-CH_3 and CH_3 absorption peaks show the same trends and the same order of change, but there are little differences between them. The Si-CH_3 peak shows a bigger change in the peak area then the CH_3 peak. The Si-CH_3 bond is probably more likely to be broken than for instance the C-CH_3 or O-CH_3 bonds. Also can be noted that the 5 sccs and the 17 sccs are closer together in figure 4.4 for CH_3 then for Si-CH_3.

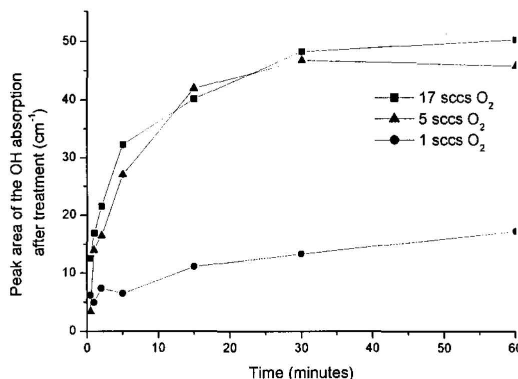

Figure 4.5: *The integrated peak area of the OH absorption peak after treatment.*

Also the oxygen related peak are investigated to check if there will be some oxygen from the plasma being built into the existing SiO_2-like film. One indication is the Si-OH peak at 3000 to 3600 cm^{-1}. Figure 4.5 shows the peak area calculated for the Si-OH absorption peak after treatment. This peak is after deposition almost not visible but grows rapidly during the post treatment. After some time then the growth slows down and it seems that this process saturates. Also it can be noted that for this parameter there is almost no difference between the 5 and 17 sccs treatment for the long treatment times. The 1 sccs curve stays far behind.

Another important absorption in the spectrum is the $SiO_{1,2}$ absorption at 450 cm^{-1}, and this bond is the most favorable for the film properties of the SiO_x-like film. For this peak the

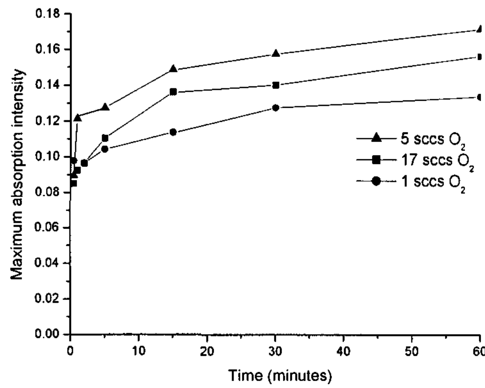

Figure 4.6: *The maximum absorption intensity of the $SiO_{1,2}$ absorption peak as a function of the treatment time.*

integrated absorption area could not be calculated while this absorptions lies on the edge of the measured absorption spectra. Often part of the absorption peak was not visible but the maximum absorption intensity though could always be determine for this absorption peak. This value however is more sensitive to noise due to the way it is determined and this method can be found in section 2.3.

The maximum absorption intensity after the treatment has been measured as a function for time and the results are given in figure 4.6. Before the treatment the maximum absorption intensity is about 0.09. The maximum absorption intensity then increases in time, but this increase slows down in time. Also for this parameter the biggest changes in the film are found with the 5 sccs treatments Furthermore it can be noted that within one hour the peak depth of the $SiO_{1,2}$ has almost doubled for the 5 sccs O_2 treatment. The 1 sccs O_2 treatment shows then a 50 % increase in the maximum absorption intensity.

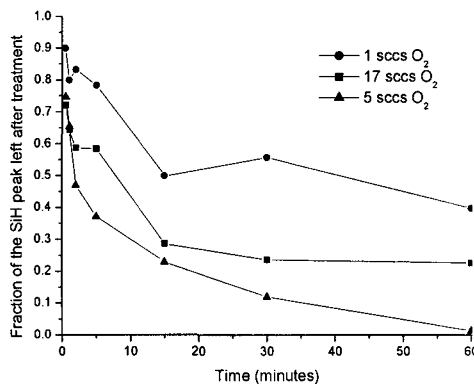

Figure 4.7: *Fraction of the SiH peak left after treatment as a function of the treatment time.*

The last absorption peak analyzed is the H-Si and H-Si-O absorption peak. Figure 4.7 shows the SiH peak area as the function of time. First it can be noted that again the 5 sccs O_2 leads to the change in the layer followed by the 17 sccs and 1 sccs O_2 flow. Again a sort of exponential decay is observed; in the beginning the changes occur much faster then after some time. Here it also must noted that the CO_2 band can interfere with the measurements and this is probably the reason for some of the odd points, i.e. noise, in figure 4.7. Compared

to the CH_3 and Si-CH_3 absorption, see figure 4.4, the SiH reduction is faster.

Discussion

The CH_3, Si-CH_3 and Si-H bonds depletion in time can be used to find the transport mechanism of the oxygen through the SiO_x films. Assume that the bond concentration is c and it is normalized to unity for the beginning of the treatment t=0. Also assume that the oxygen can move freely through the SiO_x films, and if the process is similar to an etch process, the change in the bonds Δc and the bond concentration in time $c(t)$ can be written as:

$$\Delta c = -f * \sigma * \Delta t \wedge c(t)|_{t=0} = 1 \quad (4.1)$$

$$c(t) = 1 - f\sigma t, \quad (4.2)$$

where t is the time, f the oxygen flow, and σ the reaction rate. This scenario is applicable for surface reactions or high concentrations of the bond. In this scenario the CH_3, Si-CH_3 and Si-H should reduce linear.

If the concentration of the bonds is also included in the change of bond equation 4.1 than the change of bond Δc and the bond concentration in time $c(t)$ can be written as:

$$\Delta c(t) = c * \sigma * f * dt \wedge c(t)|_{t=0} = 1 \quad (4.3)$$

$$c(t) = e^{-\sigma f t} \quad (4.4)$$

The bonds concentration now should decrease exponential. This scenario is more applicable when the oxygen can move freely through the film and the reactions take place everywhere in the film.

The bond concentration reduction found in figure 4.4 and figure 4.7 can not be reasonably fitted by equation 4.1 or with equation 4.3. Also no linear combination should be taken with equation and equation, while these would result into a non-physical solutions. With these combinations in the beginning equation 4.3 is dominant and after some time equation 4.1 becomes dominant. This is exactly the opposite of what would be expected. In this case first the bulk is changed and then the surface would be changed. Thus the assumption that the oxygen can flow freely through the film must be invalid.

If an oxygen gradient is assumed, equation 4.3 can be rewritten. In this case the concentration in the film is not only a function of the time but also a function of the depth h. Equation 4.3 can now be rewritten for this situation:

$$\Delta c(t,h) = c(h) * \sigma * f(h) * dt \wedge c(t,h)|_{t=0} = 1 \quad (4.5)$$

$$c(t) = \frac{1}{h}\int_0^h e^{-\sigma f(h) t} dh \quad (4.6)$$

For the oxygen gradient $f(h)$ various configurations can be taken. There is a large freedom in choosing the right profile to fit figure 4.4 and figure 4.7, and this has not been performed. From simulations it was concluded that the gradient must have at least a squared dependency on the height or still the figures could not be fitted.

The difference of change for each various bonds can be partially attributed to the bond strength. The bond that decreases the most is the Si-H bond then the Si-CH_3 bond and last

Table 4.4: Various bonds in the SiO film and there bonding strengths. [Verk92]

Bond type	bond strenght (kJ/mol)	Bond type	bond strenght (kJ/mol)[Verk92]
Si-Si	327	C-C	350
Si-C	414	C-O	350
Si-O	536	O-O	146
Si-H	$\leq$ 299	O-H	370
C-H	410	H-H	435
C=O	800	O-H (H_2O)	464

the CH_3 bond. As a measure for the possibility which bonds can be broken in the film for each bond the bondings strengths are given in table 4.4. In the decrease of the Si-CH_3 bonds are the breaking of the bonds between the Si and C, as well as the breaking of the C with the H or removal of the CH_3 group completely. The CH_3 absorption peak gives information about the CH_3 groups that are bonded with the Si as well as the Oxygen and other Carbons in the film. The binding strengths give the same information: the weakest bond is the Si-H and the Si-C, C-C and C-O bonds are all about the same strength. But the Si-O bond is much stronger and this could facilitate a reaction between the oxygen and the Si-C bond that breaks up the Si-CH_3 bond to generate for instance a Si-O bond.

Furthermore there are many new Si-O bonds created in the material. The $SiO_{1,2}$ bond is already an abundant bond in the deposited film and still an increase of 50% in the amount of $SiO_{1,2}$ bonds could be obtained even for low oxygen flows. Also many new O-H bonds are generated during the treatment. The O-H bonds are however not an abundant bond in the deposited films. It is likely that these OH bonds are created from the Si-H bonds in the material. The SiH bonds can be removed on three ways by oxygen:

$$\text{Si-H} + \text{O} \Rightarrow \text{Si-O-H} \quad (4.7)$$

$$\text{Si-H} + \text{O} \Rightarrow \text{Si-O} + \text{H} \quad (4.8)$$

$$\text{Si-H} + \text{O} \Rightarrow \text{Si} + \text{O-H} \quad (4.9)$$

Reaction 4.7 and 4.8 are both exotherm (based on the bond strengths) but reaction 4.9 is endotherm. Reaction 4.7 would increase peak SiO as well as peak as SiOH. Reaction 4.8 increases only peak SiO. It is believed that reaction 4.7 is dominant, because this could explain the large increase in Si-OH bonds in the film.

The methyl groups can be destroyed in many ways. Oxygen can attached itself to the methyl groups. This will destroy the methyl groups, but if the new bonds stay in the material, the Carbon concentration will not be reduced by this process, although this is not very likely. The various reactant from the Oxygen with the methyl are highly volatile species like CO, CO_2, H_2O and OH and these can be removed from the film easily. A more direct analysis technique should be used to check this.

4.1.3. Film properties versus oxygen flux

This treatment series was performed to investigate why the films treated with 17 sccs Oxygen flow show a smaller change in the properties of the SiO_x-like film then the films are treated with 5 sccs Oxygen flow. This should give some information about the reacting particle in the plasma and the type of reactions in the film. The experiments were performed as was described in section 2.3. The treatment time was 15 minutes and in this time the processes in the films have not saturated as was demonstrated in section 4.1.2.

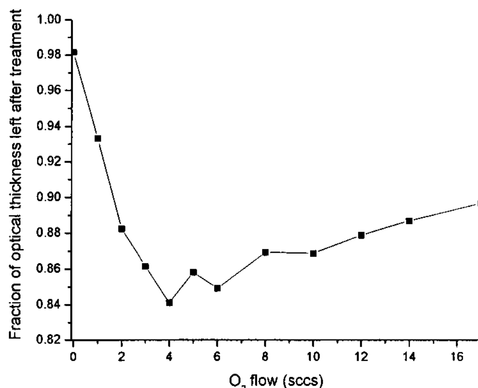

Figure 4.8: *Fraction left of the optical thickness after treatment as a function of the injected oxygen flow at the nozzle.*

Here the first parameter investigated is the optical thickness and this was measured with the FTIR spectroscope. The fraction of the optical thickness after compared to the optical thickness before treatment has been calculated for each treatment. Figure 4.8 shows the fraction left of the optical thickness after the treatment as a function of the oxygen flow through the nozzle of the arc. At no oxygen flow the optical thickness still dropped. It is believed that this could be due to oxygen leaking into the arc or plasma beam from outside the vessel. If this is true the leaks in the vessel would be about 0.3 sccs, which is rather large for a leak. Another possibility is that the Argon plasma could induce crosslinking on the surface of the SiO_x-like film. It can also be that the top of the films oxidized when they were measured *ex-situ*. But this would be more unlikely because the films were also measured *ex-situ* after the deposition, so the oxidation of the film could already have taken place. Finally it is possible that there is some residue of Oxygen inside the film or absorbed on the surface when the films were returned to the vessel for the treatment. This oxygen is then made active during the treatment, and the film is changed by this oxygen.

For low oxygen inlet the change in optical thickness is linear with oxygen flow. In this situation when more oxygen is injected in the plasma the higher the change is in the optical thickness. At an oxygen flow of about 5 sccs the change shows a maximum and if the oxygen flow is then further increased the change in the optical thickness will drop slowly again. The optical thickness can change up to 16% during the post deposition treatment for the used process parameters.

The methyl content in the layer was also measured with the FTIR spectroscope. Figure 4.9 show the reduction of the CH_3 and Si-CH_3 bonds in the SiO_x-like film. As with the optical thickness, also here is a change with no oxygen flow. For low oxygen flow, the reduction of CH_3 is linear with the oxygen flow. At 5-6 sccs the reduction of CH_3 is the largest. At

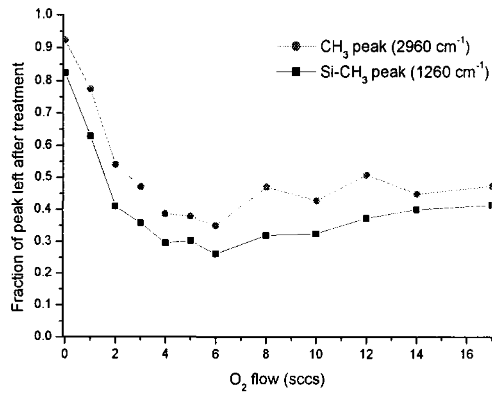

Figure 4.9: *Fraction left of the Si-CH_3 and the CH_3 absorption peaks after treatment as a function of the oxygen flow through the nozzle.*

this maximum almost 75% of the initial Si-CH_3 bonds and 65% of the initial CH_3 bonds are removed. Increasing the oxygen flow even further, the reduction of CH_3 will drop slowly.

Also it can be noted in figure 4.9 that the reduction in the Si-CH_3 peak is larger then the reduction of the CH_3 peak, as has also been shown in section 4.1.2. The bond between Si-CH_3 is more likely to be broken then the bond between C-CH_3 and O-CH_3. Not only methyl groups are broken in the film but also Oxygen is built in. To see the dependence of the OH absorption peak with the oxygen flow, the OH absorption peak was also analysed.

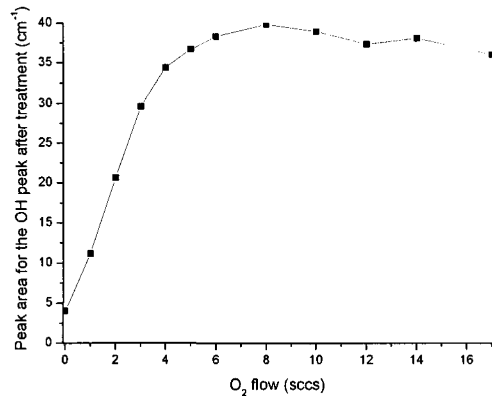

Figure 4.10: *Integrated peak area of the OH absorption peak after treatment as a function of the oxygen flow through the nozzle.*

The OH concentration is given in figure 4.10. Similar to the CH_3 concentration and the optical thickness, the changes in OH peak increases when increasing Oxygen flow, but now the maximum is less pronounced, and for a higher oxygen flow the change in the OH peak remain almost constant. Note that the amount of OH bonds in the layer does not need to be linear with the total amount of oxygen in the film. After deposition this bond is scarce in the film, but after deposition this bond seems abundant. The OH bonds is increased a factor of 8 during the treatment, but it is very unlikely that the Oxygen in the layer is also increased by the same faktor.

The absorption intensity as a function of the O_2 flow is given in figure 4.11. The same

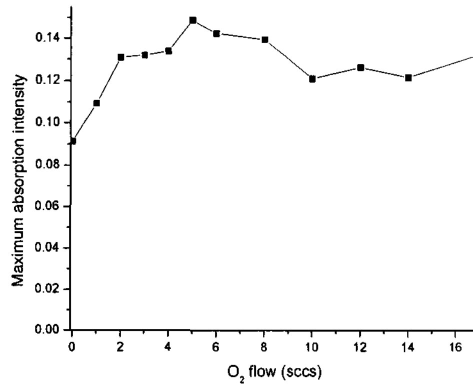

Figure 4.11: *The maximum absorption intensity of the $SiO_{1,2}$ absorption peak after treatment as a function of the oxygen flow through the nozzle.*

trend as was seen in the other measured parameters can now be recognized, except this time it is obscured by the noise. In most cases the absorption intensity increases due to the treatment at least 50%. Because the Si-O is already an abundant bond in the deposited material, this means that many new SiO bonds are formed during treatment.

The last peak that has been analyzed was the H-Si and H-Si-O peak at 2250 cm^{-1}. A part of the absorption peak overlaps with CO_2 band in the transmission spectrum. This band is due to CO_2 inside the air and in the FTIR spectroscope. The FTIR measurements were performed in normal atmosphere. Also for this peak the absorption peak area has been calculated, and the results are given in figure 4.12.

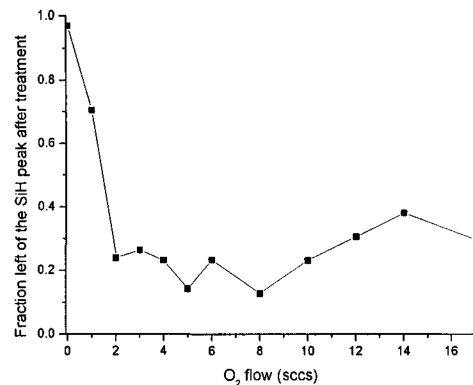

Figure 4.12: *Fraction of the SiH peak left after treatment as a function of the oxygen flow through the nozzle.*

The method for the calculation of the peak area is influenced by the shape of the CO_2 band in the spectrum, and this shape changes between the deposition and treatment, due to changes in the atmosphere inside the FTIR spectroscope. It has been shown that the breaking of the SiH bond is a fast process, see figure 4.7. The SiH reduction will therefore be already almost saturated in 15 minutes for almost all oxygen flows. Only for very low oxygen flows (< 2 sccs), the SiH reduction is not complete, and therefore the changes are already at a maximum for a oxygen flow of 2 sccs instead of the 5 or 6 sccs seen for the other parameters.

Discussion

The most remarkable result from all the measurements shown is that when increasing the oxygen flow first the changes in the film increase and when further increasing the oxygen flow, the changes show a maximum and then decrease. This maximum for a particular oxygen flow has also been observed by others in similar etch experiments [Suga98] [Brus99].

These effects are found in Reactive Ion Etch (RIE) [Suga98] or Reactive Sputter Etching (RSE) [Stei86] experiments. As a plasma Argon/Oxygen mixtures can be used and as the target often an organic polymer (C_xO_y material) is used. In these plasma the reacting particle with the polymer is O or O_2. The effect is then only observed in low-pressure plasmas (10-100 Pa), and is then contributed to the ions. For low pressure plasmas the etch mechanism is ion-assisted etching. With ion-assisted etching the excitation of the lattice caused by the ions reduces the activation energy, and therefore increasing the rate constant of the chemical reaction. For oxygen plasma when the pressure is increased, more O atoms and O_2^+ ions are created but the energy of the ions is decreased. These lower ion energies come from the lower voltage drop at the sheats, and since the mean free path of the species are inversely proportional to pressure, the lowering in potential induces a lower energy flux to the surface. The increase in O atoms and the decrease in ion energy then could result in a maximum for the etch rates at a particular oxygen flow.

With the plasma generated with the ETP setup with the cascaded arc, this scenario is unlikely. Although the pressures are in the same region there are some differences. The ETP setup is a remote plasma setup as where the plasma used for polymer etching are primarily local plasmas. The remote plasmas show a smaller voltage drop at the substrates, so the ion energy flux to the surface will be smaller, and the ions will not enhance the etch rates anymore.

Furthermore the ion flux to the substrate is less. This is because most of the O_2^+ ions are created near the arc exit. Then the plasma moves down and no (or very few) O_2^+ are created anymore. However the dissociative recombination reactions 2.7 and 2.8 of the O_2^+ ions with the electrons in the plasma will decrease the O_2^+ ion density when it is moving to the substrate. The flux of O_2^+ ions will therefore be lower compared to the flux of O_2^+ ions in a local plasma setup. Finally does the pressure in the vessel not change by more then 20 % when the oxygen flow is changed between different treatments. The Argon flow remains constant (100 sccs) for all the treatments and this flow is much greater then the oxygen flow (0-17 sccs). Because the total pressure in the vessel will not change very much, the voltage drop at the surface would also not change much. At RIE and RSE experiments, when the oxygen flow is doubled often also the pressure in the chamber is doubled and the changes in the voltage drop become higher. Although ion assisted etching could still play a role in our experiments, the effects of this process could never be as large as the measured effect of the treatment on the films.

The most likely explanation for this effect was given by Seth Brussaard [Brus99]. This effect was found when etching photoresist with Argon/Oxygen plasmas. When the oxygen is injected in the Argon plasma the Oxygen will be dissociated by the Argon ions. Although increasing the oxygen flow increases the production of O atoms, it could also decrease the flux of O atoms to the substrate. The O atom flux to the substrate does not only depend on the creation of O atoms but also on the transport of these atoms to the substrate. When the oxygen flow is low, the reaction rate of the charge exchange reaction between the argon ions and the oxygen molecules, forming O_2^+, is low. The O_2^+ then dissociates and creates O. The oxygen atoms are created all through the plasma. When increasing the oxygen flow, close to the arc more O_2^+ is formed and therefore there are less argon ions downstream in the plasma. The O atom production drops downstream and the production becomes more

Table 4.5: Various parameters used in the model

parameter	description	value
$n_{Ar^+}(0)$	normalized Argon ion flux in arc	1
k_{ce}	rate for charge exchange 2.5	10^{-16} m$^3/s$
v_d	drift speed of plasma	400 m/s
n_{O_2}	oxygen flow rate	calculated
z	distance from arc to substrate	0.6 m
$\frac{4D_O}{v_d(\rho(0))^2}$	Oxygen ambipolar diffusion constant	6.4 m^{-1}
$\frac{4D_{Ar^+}}{v_d(\rho(0))^2}$	Argon ambipolar diffusion constant	4 m^{-1}
$\frac{\phi_{O_2}}{\phi_{tot}}$	ratio of the oxygen flux to the total gas flux in arc	0/100 to 17/117
p, k, T	pressure, Boltzman constant, gas temperature	p=20 Pa, T=1500 K

concentrated near the oxygen inlet. In this case the oxygen atoms have more time to diffuse out of the plasma beam to the walls, and so the flux of O-atoms to the substrate will be lower. This is only true when the diffusion coefficient of the oxygen atoms is greater then the diffusion coefficient of the argon atoms. Here as a first guess it is assumed atomic oxygen diffusion coefficent is approximately 1.6 times higher then the diffusion constant of Argon. This assumption is based on that the diffusion coefficient would be at some degree inversely linear with the square root of the mass of the atom. This is in contradiction of the atomic oxygen diffusion constant taken by Brussaard where a much higher diffusion constant is taken. In the model the normalized atomic oxygen flow at the substrate as a function of the oxygen flow can be calculated with the following equations:

$$n_O(z) = 2n_{Ar^+}(0)k_{ce}\frac{1}{v_d}\int_0^z \frac{\exp\left(-n_{O_2}k_{ce}\frac{1}{v_d}z'\right)}{\frac{4D_O}{v_d(\rho(0))^2}(z-z')+\frac{4D_{Ar^+}}{v_d(\rho(0))^2}(z'+1)}dz' \quad (4.10)$$

$$n_{O_2} = \frac{\phi_{O_2}}{\phi_{tot}}\frac{p}{kT}, \quad (4.11)$$

where the used parameters are described in table 4.5.

Three different cases for the model can be identified. If the diffusion coefficient is the same for both argon and oxygen, the integral can be calculated and the normalized oxygen flow to the substrate will be like $a*(1-exp(-b*n_{O_2})$, where a and b are positive constants. The atomic oxygen flow at the surface would saturate when increasing the molecular oxygen flow at the nozzle. When the diffusion coefficient of Argon is higher then the diffusion coefficient of Oxygen, the normalized atomic oxygen flow at the surface will always increase when increasing the molecular oxygen flow at the nozzle. When the diffusion coefficient of the oxygen is higher then the diffusion coefficient of Argon, the atomic oxygen flux will show a maximum when increasing the molecular gas flow at the nozzle and then when increasing the molecular oxygen flow even more, the atomic oxygen flow at the substrate will drop.

Table 4.5 shows also the values used for the calculations of equation 4.10. The values used are mostly estimates for the different parameters and there is some freedom in choosing the values. Note that for instance the molecular oxygen flow n_{O_2}, the drift speed v_d and the reaction rate k_{ce} are all dependant in equation 4.10. Therefore no fits with the simulation on the measured data have been performed. With these values given, the normalized atomic oxygen

flux $n(z)$ at the substrate as a function of the oxygen flow at the nozzle can be calculated. The result of this calculation is given in figure 4.13.

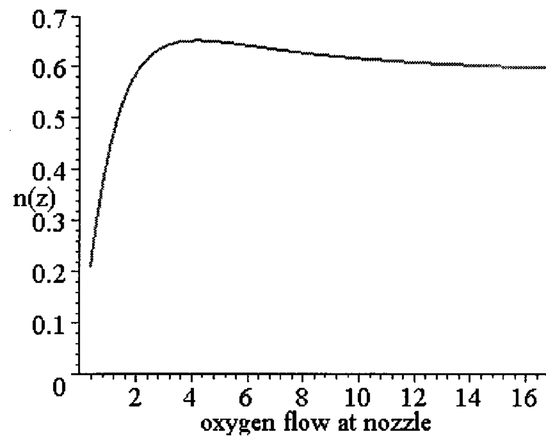

Figure 4.13: *The atomic oxygen flow at the substrate n(z) as a function of the molecular oxygen flow at the nozzle.*

For low oxygen flows in the nozzle $n(z)$, the atomic oxygen flow at the substrate is linear with the oxygen flow in the nozzle. When increasing the oxygen flow at the arc the atomic oxygen flow at the substrate will show a maximum and then drops. These simulations show the same profiles as the measured changes in the properties of the film. When the reactions of the oxygen atoms with the CH_3 groups in the SiO_2-like film are flux driven, then the change in the CH_3 groups should have the same profile as figure 4.13. In the optical thickness the effect is even enhanced. As well as the refractive index as the thickness of the layer are changed by the post treatment. If both changes are flux driven, the graph profile of the change in optical thickness is then squared and the drop for high oxygen flows would become more visible.

Due to the large changes in the film the reacting particle in the plasma should be abundant in the plasma. Two candidates remain: molecular and atomic Oxygen. If the molecular oxygen would be the reactant species no reaction profiles as given in i.e. figure 4.8 could be obtained. With molecular oxygen the oxygen flow at the substrates would be linear with the oxygen flow at the nozzle, and the changes in the films should be linear with oxygen flow or possible saturate for high oxygen flows, but no drop should occur when increasing the oxygen flow. So it can be concluded that the reacting particle of the plasma is O. In other similar processes it was also found that the reacting particle was O [Suga98].

4.2. Fast grating infrared spectroscopy

Several experiments have been performed with the new Fast Grating InfraRed Spectroscope (FGIR) to check the performance of the setup. A gas absorption measurement has been performed as a mean to calibrate the wavelength dependence of the setup. Depositions have been performed on Si substrates as well as on a ZnSe ATR crystal to further characterize the setup. Absorption spectra of the SiO_2-like films were measured and the sensitivity of the FGIR setup was checked.

4.2.1. Gas/reflection

The first test for the setup was to measure the absorption spectrum of Hexamethyldisiloxane (HMDSO) gas. The HMDSO gas absorption experiment was also peformed with the FTIR spectroscope, and both results can be compared. In this way the wavelength of the system can be calibrated. When setting up the spectroscopy the grating cannot be set on exactly the same position every time. This way the exact angle of incident and the diffracted angle become unknown. An error of 1 degree in both angles can lead to an error in the wavelength of 5%. Furthermore, the angles are difficult to measure because the path the light travels cannot be seen by the eye. If the system is uncalibrated only the absorption spectra can be measured in units of rotation of the grating. To do a calibration at least two points in the absorption spectrum must be identified and the corresponding wavelengths should be known. With these two or more points the angle of incident and the diffracted angle can be calculated. From this the rotation angle on the x-axis of the intensity spectra measured by the FGIR setup can be exchanged by wavelength units with equation 3.1.

For this experiment the setup was build around the depo 1 setup, and was aligned to maximize the signal on the MCT detector. A Si substrate was put into the vacuum chamber and the vessel was pumped down to a base pressure of $4*10^{-5}$ mbar. Then the vacuum pumps were closed and HMDSO gas was let slowly into the vessel. As a carrier gas for the HMDSO, Argon was used, with a ratio of 2:1 (HMDSO/Argon). The total pressure rose to 1 mbar within 30 seconds. During this time the setup was measuring the emission/absorption spectra. The grating frequency was set at 75 Hz and the ADC was sampling at 150 kHz. Notice that for each grating period two spectra can be measured, one forwards and one backwards.

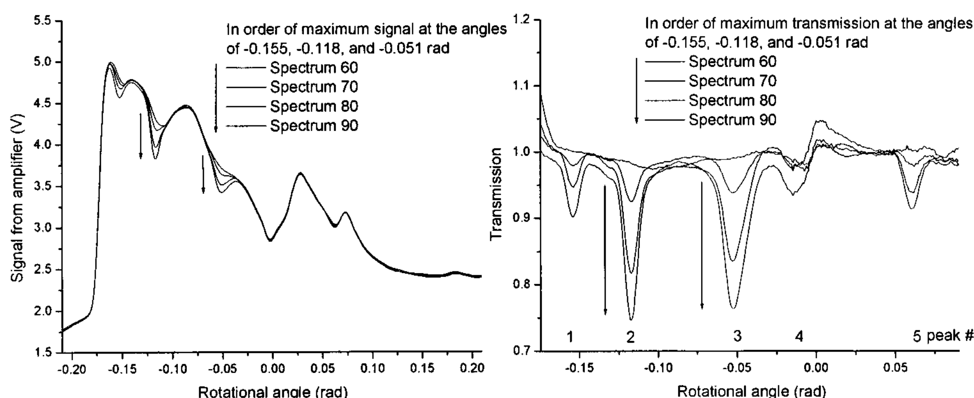

Figure 4.14: *On the left side the signal measured from the detector as a function of the rotational angle of the grating and on the right the calculated transmission spectra.*

Figure 4.14 shows some intensity spectra measured during the experiment. The spectrum with the overall highest intensity is the intensity spectrum for a measurement with no HMDSO gas in the chamber. For a rotation angle of -0.22 to -0.18 rad no light from the arc is detected, only background light. At -0.18 rad the cut off edge from the filter is observed and also light coming from the arc is observed. From -0.18 to 0.10 rad the shape of the intensity spectrum seems to resemble the emission spectrum of the cascaded arc with the cut off filter as seen in figure 3.3 in section 3.2.

When the HMDSO gas pressure increases in the chamber the light intensity spectrum starts to change. For instance at a rotational angle of -0.155 and -0.118 rad the light intensity drops quite fast although at -0.07 rad the light intensity stays almost the same during the measurement. The total gas pressure at the end of the experiment was about 1 mbar, and the HMDSO gas pressure would be approximately 2/3 of the total gas pressure.

Also it should be noticed that the y-axis in figure 4.14 is no absolute scale for the light intensity. The MCT detector also measures infrared light that does not come from the arc but from all the objects in the room that radiate heat. This light can be measured by switching of the arc and measuring the signal on the detector also as a function of rotational angle of the grating, and this spectrum is called the background light spectrum, and the result is given in figure 4.15

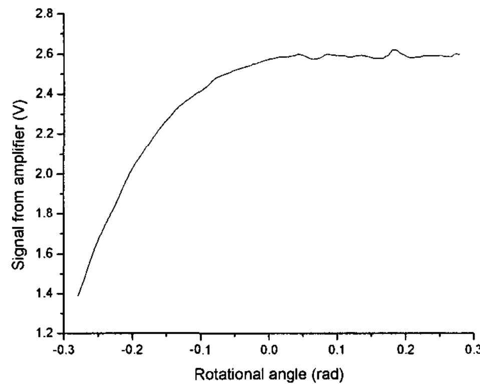

Figure 4.15: *The background light measured with the setup.*

When this background light spectrum is subtracted from the measured signal on the detector when the arc is switched on, the intensity of the light coming from the arc is obtained as a function of the rotation angle of the grating.

The absorptions in the intensity spectra can be made clearer in a transmission spectrum. Here the intensity spectra are divided by the first intensity spectrum measured, called the reference spectrum. So for each spectra measured first the background light spectrum is subtracted from the spectrum and then it is divided by the reference spectrum. The right side of figure 4.14 shows the absorption spectra generated this way. The first spectrum measured is used here as the reference spectrum. In these absorption spectra 5 peaks can be located at -0.155, -0.117, -0.052, -0.014, and +0.060 rad.

The absorption spectra were then compared with the absorption spectra that was measured with the FTIR spectroscope. In this experiment the HMDSO pressure was about 0.7 mbar, and thus the absorption intensities cannot be compared only the location of the various absorptions. The result from those measurements are given in figure 4.16 [Hest98].

In this spectrum 5 distinct peaks can be observed (1260, 1073, 850, 758, and 689 cm^{-1}).

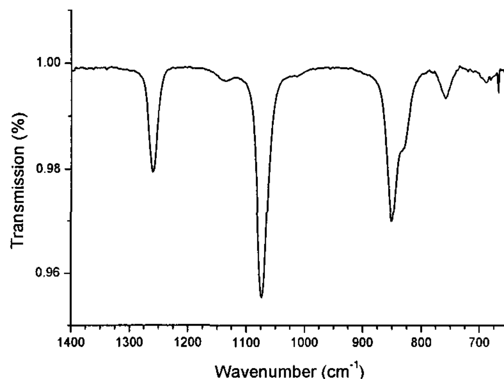

Figure 4.16: *HMDSO gas phase absorption measured with the FTIR spectroscopy.*

Table 4.6: Possible assignment for the peaks measured for the HMDSO gas absorption experiment

Peak number	rotational angle (degree)	possible peak (cm^{-1})	possible peak (μm)
1	-0.155	1260	7.94
2	-0.117	1073	9.32
3	-0.052	850	11.76
4	-0.014	758	13.19
5	+0.060	689 / 2nd order 1260	14.51 / 15.9

When comparing both spectra, a possible assignment of the absorption peaks in figure 4.14 can be made. A possible configuration is given in table 4.6.

When the assignment is correct the rotational angles in figure 4.14 can be converted to wavelength. To transform the rotation angle in the x-axis to wavelenghts the incident and diffracted angle on the grating should be known. The angle of incident θ_i [rad] of the light on the grating and diffracted angle θ_m [rad] of the setup can be calculated in the following way. First the wavelength of the assigned peak is plotted as a function of its corresponding rotational angle α [rad] , as seen in figure 4.17. In figure 4.17 the black dottes are the possible peaks positions with their corresponding wavelength. Now this graph can be fitted with the following equation to find the incident and diffracted angle (definition of the parameters analog to equation 3.1):

$$a(\sin(\theta_i + \alpha) + \sin(\theta_m + \alpha)) = m\lambda \tag{4.12}$$

As fit parameters the incident angle and the diffracted angle are used (a=20 μm, m=1, λ is in μm). The fitting is shown in figure 4.17 as a line.

The fit parameters θ_i and θ_m where determined and found to be 0.133 and 0.585 rad, respectively. In this fit the lower point at 0.1 rad (peak 5) was not taken into account. This point is clearly not on the same line as the rest of the points. Peak 5 therefore does not corresponds with the peak at 689 cm^{-1}. Another possibility is that this is light diffracted into the second order, then the peak correspondes to a wavelength of 7.8 μm, which would then the same as absorption peak 1. Because the size of peak 1 and peak 5 are almost the same it is therefore assumed that absorption peak 5 is the second order of the diffraction peak at 1260 cm^{-1}. The corresponding point in figure 4.17 coincides with the fitted line, which proves it is a second order feature. With this information figure 4.14 can be replotted but now with

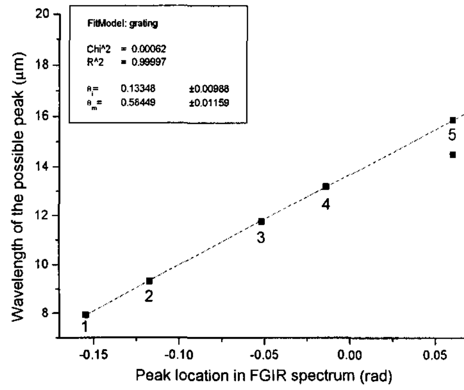

Figure 4.17: *The peak location (in rad) of the absorption peaks in the FGIR transmission spectra with the corresponding absorption peak wavelength that was assigned to it.*

the wavelength or wavenumber on the x-axis, and the result is given in figure 4.18.

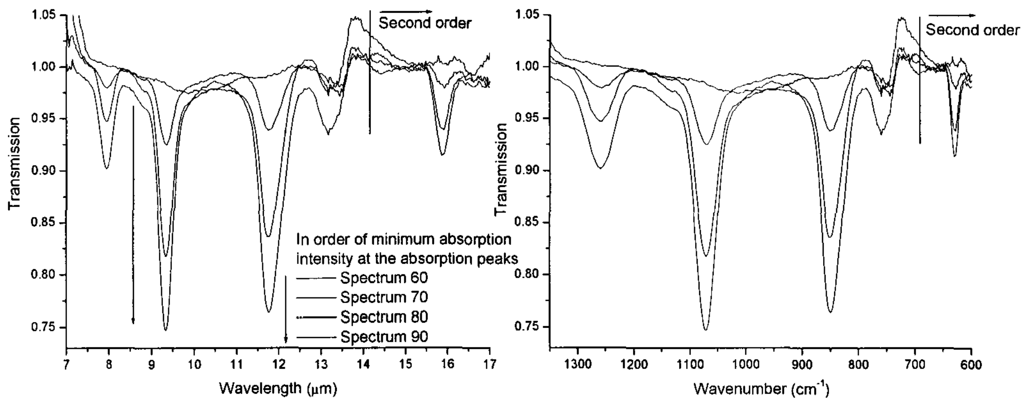

Figure 4.18: *The transmission spectra of HMDSO gas with wavelengths (left) and wavenumber (right) as x-scale.*

Now the spectra from figure 4.18 and figure 4.16 can be compared. Above 1400 cm^{-1} the absorption spectrum is noise because the filter cuts off all the light above 1400 cm^{-1}.The absorption spectrum above 14 μm or below 714 cm^{-1} can be disturbed by second order diffractions. When comparing the transmission spectra obtained with FTIR and FGIR, the first thing to notice is that the resolving power with the FTIR is much higher then the grating spectroscope. It is assumed that the resolving power of the FTIR spectroscope is high enough such that the measured absorption peaks are not broadened. Then the resolving power of the FGIR setup can be estimated from the widths of the absorption peaks and the resolving power is approximately 40 at 10 μm, and this is almost the same as was calculated in the design of the setup in section 3.4.

4.2.2. Deposition

The goal of the setup was to measure monolayer absorptions during the deposition of SiO_2-like films with use of a Attenuated Total Reflection (ATR) crystal. But first a deposition on a Si wafer has been performed, i.e. only the absorptions for a single reflection on the sample were measured. The measured light intensity will be larger than with an ATR but the absorptions will be smaller. The deposition was performed to investigate if the characteristic absorption spectrum of the SiO_2-like film could be measured. The main absorption peaks of the SiO_2-like layer in the region of 700 cm^{-1} of 1430 cm^{-1} are: the $SiCH_3$ vibration mode at 1250 cm^{-1}, the Si-O-Si stretching vibration with the Si-O-C vibration mode at 1030 cm^{-1}, and the absorption band of Si-$(CH_3)_{1,2,3}$ at 800 cm^{-1} to 850 cm^{-1}. A typical absorption spectrum for the SiO_2 like film measured with the FTIR, in the range of interest, is given in figure 4.1 in section 4.1.

Before the deposition an HMDSO gas phase absorption calibration had been performed and the angle of incident and the diffracted angle found were 0.0077 rad and 0.657 rad respectively. The grating frequency was set at 75 Hz and the sample frequency of the ADC was 150 kSample/s. Before the deposition a intensity spectrum was measured when the arc was switched off. This was to measure the background light. After the background intensity spectrum was measured, the deposition of the SiO_2 was started.

The deposition was performed under "standard conditions", which are given in table 2.1 in section 2.3. The deposition took about 50 seconds and during deposition 7500 absorption spectra were measured. During the deposition the sample was monitored not only with the Fast Grating InfraRed (FGIR) setup but also with ellipsometry. From the ellipsometry data it was concluded that the final thickness of the layer was approximately 1 μm and the growth rate of the layer was 20 nm/s.

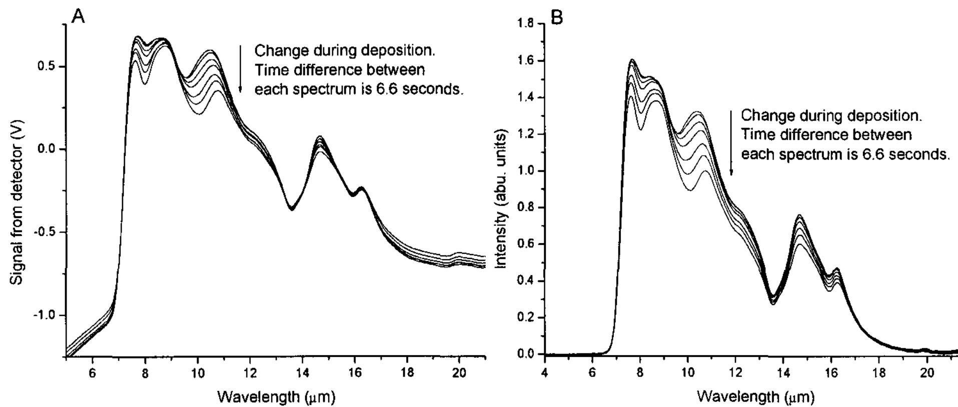

Figure 4.19: *Signal from the detector and the measured light intensity as a function of the wavelength.*

Figure 4.19 shows some of the measured intensity spectra during the deposition. The angles are already converted to wavelengths with equation 4.12. Between each spectra shown in figure 4.19 there is a time difference of about 6.6 seconds. Now the shape of the intensity spectra can be understand. Below 7 μm no light can reach the detector. From 7 μm to 14 μm the shape resembles the shape of the emission spectra of the arc with the cut-off filter in front as can be seen in figure 3.3 in section 3.2. At 14 μm the second order appears and this order should be visible to about 21 μm. This however is not, and this can be attributed to the blaze angle. The blaze angle is optimized to diffract light with a wavelength of 10 μm in the first

order. The reflection of the grating for the angles used to get 23 μm light is low, and the cut off of the reflection due to the blaze angle is at about 19 μm.

In figure 4.19 it has to be noted that the absolute/overall intensity for all wavelengths seems to shift/drift. The drift in the intensity can probably be attributed to the detector. The drift was eliminated by adding or subtracting an offset to the signal. This offset was chosen in such a way that the intensity spectrum would overlap with the background intensity spectrum for wavelengths below 7 μm. Below 7 μm the cut off filter will block all the light from the arc, and only background light will reach the detector. The measured intensity spectrum and the background light intensity spectrum should therefore be the same for the spectra below 7 μm. When the drift is eliminated this way all the intensity spectra also overlap for wavelengths above 20 μm as can be seen on the right in figure 4.19. Because the intensity spectra overlap for wavelengths for wavelengths below 7 μm as well as above 20 μm when adding or subtracting a offset to the signal, it is assumed that this technique is valid. This drift was also already been seen in the gas absorption measurement, but their it was less visible.

The absorption spectra of the SiO_2-like layer are obtained by dividing all the intensity spectra by a intensity spectrum of a clean Si sample when no deposition was started. Figure 4.20 shows some of the absorption spectra measured this way during the deposition.

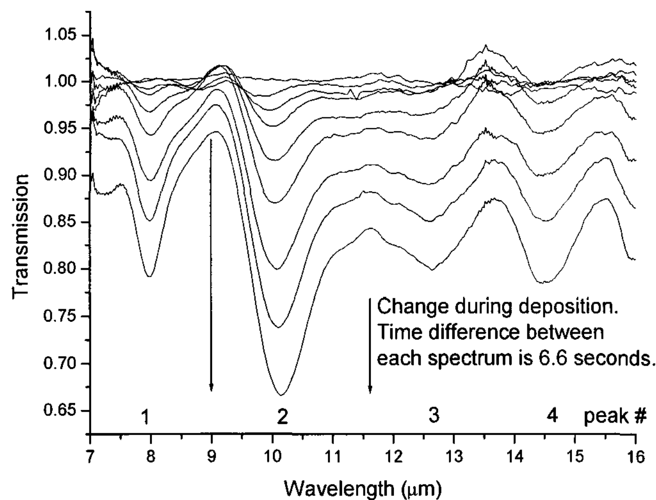

Figure 4.20: *Calculated transmission spectra during deposition.*

A few things can be noted in figure 4.20. First the general reflection for all wavelengths seems to drop during the deposition. The whole absorption spectra are lowered. This reduction in total transmission can also be due to interference in the film. Furthermore four distinct absorption peaks can be identified in the spectra seen in figure 4.20. These absorption peaks then can be assigned to the typical absorption peaks in the SiO_2-like absorption spectrum. Table 4.7 shows the location of the peak and which vibration mode is assigned to it.

The fourth peak is a ghost/artificial absorption. This is an attribute of the cut-off filter. The peak lies between 13.6 μm and 15.4 μm. This is the second order of 6.8 μm and 7.7 μm and this is exactly the range of the cut-off edge of the cut-off filter. If the location of this edge shifts only a little when it gets divided by the first spectra an absorption like peak will appear in the transmission spectra.

The locations of the assigned absorption peaks seems to coincide nicely with the measured absorptions as can be seen in table 4.7. Any differences can be attributed to the higher

Table 4.7: Absorption peaks of a typical SiO-like film.

#	Peak location in wavelengths	Possible absorption [Cour97]
1	8.00 μm [1250 cm^{-1}]	Si-CH_3 vibration mode at 1260 cm^{-1}
2	10.17 μm [983 cm^{-1}]	Si-O-Si stretching vibration mode at 1030-1070 cm^{-1}
3	12.67 μm [789 cm^{-1}]	Si-$(CH_3)_{1,2}$ / Si-$(CH_3)_3$ vibration mode at 800-850 cm^{-1}
4	14.50 μm [690 cm^{-1}]	Second order effect of 1250 cm^{-1}

resolution of the FGIR sectroscope compared to a typical FTIR spectroscope. Also here the transmission spectra are measured in reflection mode instead of transmission mode. This also could lead to a change in the wavelength of the location of the maximum absorption intensity.

As a test to see if the assignment is valid a post deposition treatment experiment was performed on the deposited film. In this experiment the sample was exposed to an Argon/Oxygen plasma. The plasma process parameters are given in table 4.1 in section 4.1. The time of the post treatment was 10 minutes. From the result from section 4.1.1 it was shown that this plasma would reduce the Carbon concentration and increase the Oxygen concentration in the film. So the 1260 cm^{-1} Si-CH_3 and the 800-850 cm^{-1} Si-$CH_{1,2,3}$ absorption peaks has to decrease in size and that the 1030 cm^{-1} Si-O-Si absorption peak has to increase in size. To reduce the amount of data that would be measured, the grating frequency was set to 4 Hz and the ADC sample frequency to 16 kSamples/s.

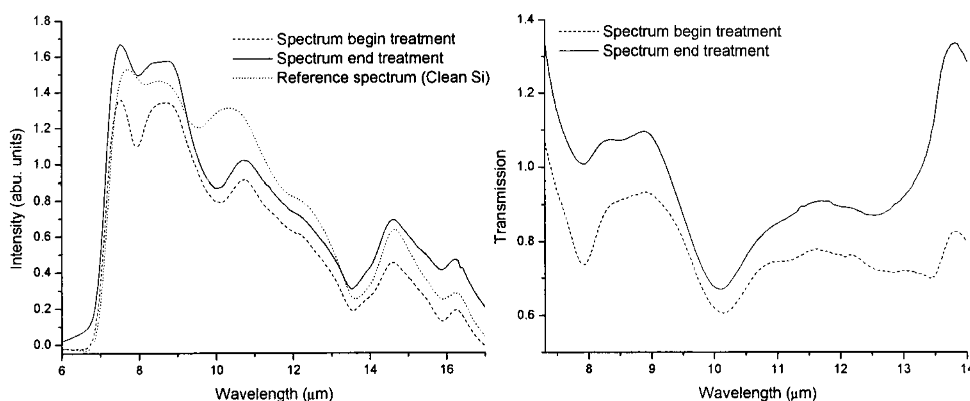

Figure 4.21: *Intensity spectra and the calculated transmission spectra before and after treatment.*

The intensity spectra measured in the beginning and the end of the etch as well as the spectrum measured with the clean Si-sample are given in figure 4.21 on the left. In figure 4.21 on the right the corresponding absorption spectra are given. The first thing to notice is that the transmission spectra are distorted. There are two possible reasons. The first is that the reactor has become hot and starts to radiate more infrared light, which would interfere with the measured intensity spectra. Another possibility is that the distortion is due to a minimal change in position of the grating. This change in angle can already be seen in the intensity spectra. The location of the cut-off edge of the cut off filter moved to a higher wavelength, which is physically very unlikely. Thus it must be concluded that the calibration of the FGIR setup is not valid anymore, and in principle a new calibration has to be performed. If it is assumed that the incident angle changed by 1.5 mrad, the location of the cut-off edges are moved back on the right place and the absorption can be calculated again. The change in the

incident angle can be due to mechanical vibrations. The optical setup is placed on a table attached to the vacuum chamber. Now mechanical vibrations from the vacuum system can interfere with the position of the grating. The new absorptions calculated with a change in the incident angle of 1.5 mrad are given in figure 4.22.

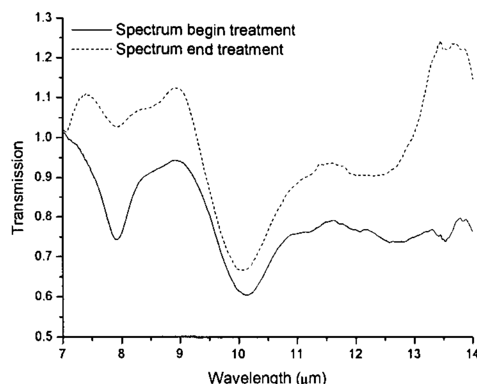

Figure 4.22: *Recalculated transmission spectra before and after treatment.*

The new absorption has been improved for for the range of 7 to 12 μm but then other artificial peaks appear. But still the absorption spectra are good enough to notice that the peak at 8 μm decreased in size and the peak at 10 μm increased in size. Therefore it can be concluded that the peak at 8 μm is in fact the Si-CH_3 peak and the peak at 10 μm is the Si-O-Si peak. The change in size of the peaks at 8 and 10 μm can also already be seen in figure 4.21 A and are not merely mathematical artifacts when translating the spectra.

It was calculated in section 3.3 that the absorption peaks detected need to be at least about 1 % to be detected. This can also be seen in figure 4.20. Absorptions peak below 1% are obscured by the noise in the measurements. A film of 1 μm thick generates a maximum absorption intensity of 35% as can be seen in figure 4.20 and a absorption of 2% can be detected, then the sensitivity of the FGIR setup is about 30 nm. This is when no transmission spectra are averaged. Note that averaging the spectra would increase the measuring time for one spectrum of the setup, which is undesired. To improve the sensitivity of the FGIR setup an ATR crystal can be used.

4.2.3. ATR

The Attenuated Total Reflection (ATR) technique is often used to measure the very small, monolayer absorptions [Bruk97]. With the ATR crystal the pathlength the light moving through the layer of interest is increased. This can increase the size of the absorptions with at least one order of magnitude. The ATR crystal used is a 0.5 mm x 1 cm x 50 mm ZnSe crystal. The angle of incident is 1.13 rad. The number of reflections on the top plane can be calculated by equation 3.11 and is about 35. The ATR crystal can be used in the region of 600 cm^{-1} to 20.000 cm^{-1} because it has a low absorption coefficient for the infrared light. The refractive index is 2.4 and the reflection loss at the surface is 30% [Bruk97]. Furthermore it has a high resistance to chemical attacks, which should make it easy to clean, so it can be reused.

Only one deposition has been performed on the ATR crystal. The deposition parameters are given in table 2.1 in section 2.3. The deposition time was 50 seconds and a layer of 1 μm of SiO_2-like material was deposited. The main problem that will arise with ATR is the lower signal intensity as can be seen when comparing figure 4.23 with figure 4.19. In these measurements the same amplification factor for the amplifier of the detector has been used. The signal strength dropped from 1.7 V to 0.35 V. This drop is in the order as was calculated in section 2.4. The drop in intensity will decrease the signal to noise ratio of the setup. The main loss of light intensity is in the focusing of the light into ATR crystal. The spot size of the light beam is much larger than the entrance of the ATR crystal. The spot size is about 6 cm in diameter and the entrance of the ATR crystal is 2 cm by 0.6 cm.

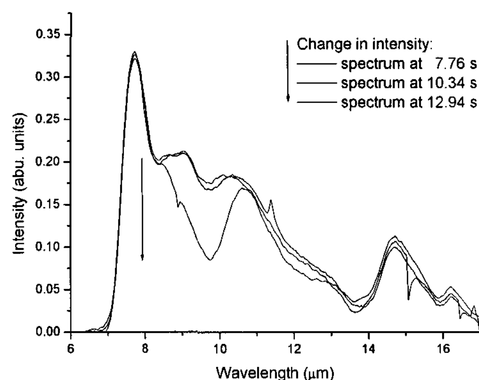

Figure 4.23: *Intensity spectra during deposition on a ATR crystal.*

Figure 4.23 shows three of the intensity spectra measured. It can be noted that the signal varies rapidly in the range of 7 to 8 *μm*. A small error in the measured angle of rotation of the grating will lead here to great errors for the calculated absorption spectra. Furthermore some spikes appear in the measured signal. A possibility is that these spikes come from the starting of the plasma.

Figure 4.24 shows some of the calculated absorption spectra. Between 5.1 and 7.7 seconds the deposition started. In 2.6 seconds the maximum Si-O-Si absorption peak intensity at 9.7 μm increased from 0.1 to 0.5. The absorptions in the transmission spectra grow much faster with the ATR crystal in use compared to the depositions with only a Si-substrate. In figure 4.20 the last spectrum was for a film thickness of 1 μm and the maximum absorption intensity was 0.35. With the ATR the absorption peak grows already to a maximum absorption intensity of 0.5 after approximately 3 seconds of deposition. In this time only a film of 60 nm could be

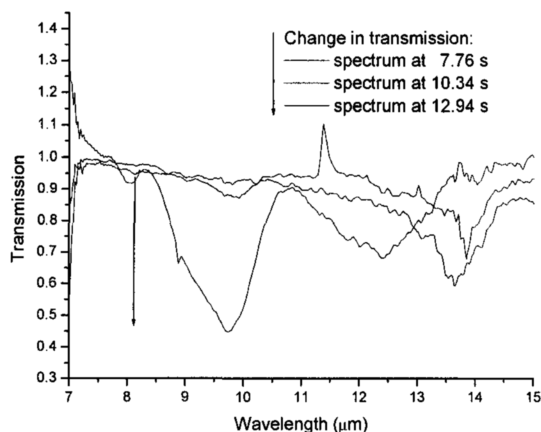

Figure 4.24: *Transmission spectra obtained during deposition on an ATR crystal.*

deposited. The absorption peaks at 9.7 μm (Si-O-Si) and 11.7 μm to 12.5 μm ($(Si\text{-}CH_3)_{1,2,3}$) are clearly visible, but the $Si\text{-}CH_3$ absorption peak at 8 μm is not nearly as strong as the other peaks.

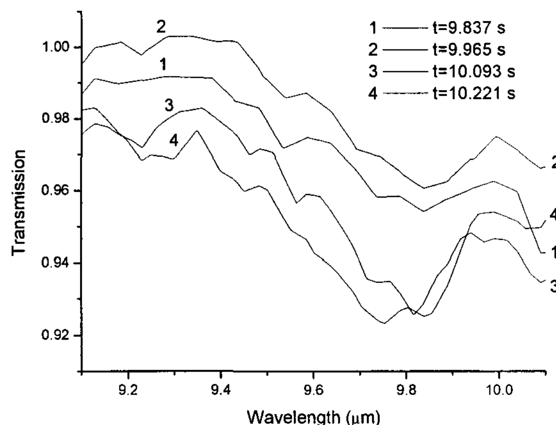

Figure 4.25: *Transmission spectra obtained during deposition on an ATR crystal within 0.5 seconds during the start of the deposition.*

Figure 4.25 shows some of the measured Si-O-Si absorption peaks a few moments after deposition. Because of the low light intensity detected the noise on the spectra is large (1% to 2%). To see if the absorptions grow the area of the absorption peak is determined. To do this a straight line from the right top to the left top was drawn and the area between the line and the absorption spectra was calculated. The result are given in figure 4.26.

Due to the technique use to find the peak area even when there is no absorption a non-zero peak area will show. Round about 9.9 seconds after the measurement was started the deposition begun. For the deposition parameters used the grow speed of the layer is 20 nm/s. One monolayer of SiO_2 is 3 Å thick. So 1 monolayer is deposited every 30 ms. In figure 4.26 in a time period of 0.1 second a significant change in the peak area of the Si-O-Si absorption peak can be detected. So a 2 nm SiO_x film could be detected by the setup. This is however thicker than one monolayer. Thus the setup still has to be improved to meet its original goal of monitoring in-situ the film growth with monolayer sensitivity. Also must be noted here

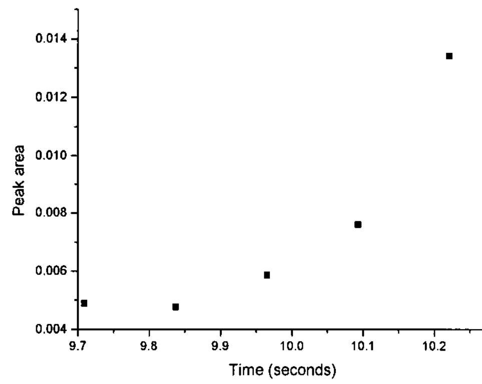

Figure 4.26: *The calculated absorption peak area for the Si-O-Si peak for the spectra just before and after the deposition started.*

that the sensitivity of the setup is calculated for the Si-O-Si bond which has the strongest absorption in the transmission spectra. To be able to detect the other bonds in the film, the film needs to be thicker.

5. Conclusions and Future directions

5.1. Post deposition treatments

The changes in the films during the treatment were observed and found to be substantial. Even for short treatment times, one or two minutes, the amount of bonds changed significantly, often about 10% or 20%. From the treatment series that investigated the film as a function of the treatment time it can be concluded that the oxygen must diffuse into the film and that is a slow process and first the top of the SiO_x-like film is changed and then the bulk. In this series it was also observed that the changes in the film were not linear with the oxygen flow injected into the plasma.

Therefore another treatment series was measured to find the dependency of the processes in the film with the oxygen flow. Here it was found that the films change most when the oxygen flow through the nozzle was approximately 5 or 6 sccs. When the oxygen flow was then increased the changes were less. This behavior was attributed to the atomic oxygen flux impringing at the surface. This parameter was not linear with the molecular oxygen flow through the nozzle, but when using the model of Brussaard, this parameters showed the same behavior as a function of the oxygen flow through the nozzle, as the film properties. From this it was concluded that the reacting particle was atomic oxygen.

For the 500 to 700 nm thick layers it was found that it takes a long time (>15 minutes) before more then 50% of the layer is changed, and therefore this process can not be used to improve the film properties of thick SiO_x-like films (>300 nm). If the Carbon concentration in thick films needs to be changed, then it has to be done during deposition. Every so often during the deposition, the deposition needs to be stopped and a short treatment can be performed to reduce the carbon in the films. Then the deposition can be started again and this process of deposition and treatment can be repeated again. This would then however reduce the effective deposition rate of the setup drastically.

It could possible that that when a methyl bond is destroyed, the Carbon still stays in the film. However these newly created carbon bonds would be noticed in the FTIR measurements and this was not. But still it would be preferable that the treated films are analyzed with a different technique to find the exact Carbon concentration in the films after treatment.

5.2. FGIR

The Fast Grating InfraRed (FGIR) spectroscope has been designed, build and tested. In the design it was found possible to build a tool that could meet the needs that were stated for the setup. It can measure 1% absorptions on a timescale less then 10 ms. If compared to an FTIR it was found that the measuring range for the FGIR setup is lower (7 μm to 14 μm). Also the resolving power is lower, a resolving power of 40 at 10 μm can be obtained with the FGIR setup compared to a resolving power of at least 100 for a typical FTIR spectroscope. The resolution of the FGIR setup is in the same range as an FTIR spectroscope and is at most 8

cm^{-1}. The FGIR setup has been tested with a HMDSO gas absorption measurement, and two SiO depositions; one with a substrate and one with a ATR crystal. In all these measurements, the absorption peaks could be found and identified. It was also found that the resolving power was high enough so that different absorption peaks do not overlap. With the deposition the characteristic absorption peaks could be measured and analyzed. It was found that FGIR setup has a low sensitivity when a Silicon substrate is used (single reflection). The absorption of a 30 nm thick film can be measured. Thus an ATR crystal was used to measure monolayer depositions. The ATR reduces the measured intensity by a factor of 6 and the signal to noise ratio is increased. With the ATR crystal absorptions of 2 nm can be detected. If the light intensity is increased the FGIR setup the sensitivity could be further increased. This can be done by increasing the pressure in the arc. Also the noises in the setup can be reduced which will further increase the sensitivity. Noises in the background can be reduced by using a cold shield in front of the detector. Also the optical elements of the FGIR setup can be placed in a more stable way, so they are not sensitive to vibrations in the deposition tool.

The occurrences of ghost absorptions were observed in the longer measurements, and these were attributed to changes in the alignments during the measurements. Finally it must be said that when aligning the setup much care must be taken. The resolving power and signal to noise ratio of the setup is dependant of a proper alignment.

BIBLIOGRAPHY

[Adam83] A.C. Adams, Solid State Technology, **1983**, *vol 26*, 135

[Boer95] H.J. Boer, Journal de Physique IV, Colloque C5, Suppl. Journal de Physique II, **1995**, *volume 5*, 961-967

[Boga95] K.H.A. Bogart, N.F. Dalleska, G.R. Bogart, and E.R. Fisher, Journal of the vacuum science and technology A, **1995**, *13*, 476-480

[Born99] *Principles of optics*, 7th edition, Born & Wolf, **1999**, Cambridge university press

[Bruk97] *FTIR instruction course notes on ATR*, Bruker, 1997

[Brus99] *Remote arc generated plasma in diatomic gases*, Seth Brussaard, **1999**, Ph.D. Thesis, Eindhoven university of technology

[Camb96] *Instruction manual of the optical scanner*, **1996**, Cambridge technology incorporated

[Char92] C. Charles, P. Garcia, B. Grolleau, and G. Turban, Journal of the vacuum science and technology A, **1992**, *10*, 1407-1413

[Cour97] *Infra-Red absorption spectroscopy of SiO_2 deposition plasmas*, C. Courteille, D. Magni, A.A. Howling, V. Nosenko, and C. Hollenstein, 40th Annual technical conference proceedings, **1997**, ISSN 0737-5921, Society of vacuum coaters

[Harr67] *Internal reflection spectroscopy*, N.J. Harrick, **1967**, John Wiley & Sons, Inc

[Heme01] *Design of a mid-infrared cavity ring down spectrometer*, Marcel Hemerik, **2001**, Ph.D. Thesis, Eindhoven university of technology

[Hest98] *Infrared spectroscopy and mass spectroscopyon expanding Ar/C_xH_Y plasmas*, M.F.A.M. van Hest, **1998**, Master Thesis, Eindhoven university of technology

[Hove97] *In situ temperature and a-Si:H deposition measurements with a rotating compensator ellipsometer*, Bart Hovens, **1997**, Master. Thesis, Eindhoven university of technology

[Hurt92] *Diffraction gratings*, M.C. Hurtley, **1982**, Academic Press

[Giel96] *Plasma beam deposition of amorphous hydrogenated Carbon*, J.W.A.M. Gielen, **1996**, Ph.D. Thesis, Eindhoven University of Technology

[Graa00] *Deposition of CNH Materials: Plasma and film characterization*, A. de Graaf, **2000**, Ph.D. Thesis, Eindhoven University of Technology

[Have89] *In situ measurements of C_nF_m densities in an RF CF_4 plasma using infrared absorption spectroscopy*, M. Haverlag, G.M.W. Kroesen, F.J. de Hoog, **1989**, Proceedings of the 9th International Symposium on Plasma Chemistry, University of Bari, Bari, p 441-445

[Jans96] *Deconvolution of images and spectra*, P.A. Jansson, **1996**, Academic press, San Diego

[Kash91] *Hybrid films formed from hexamethyldisiloxane and SiO by plasma process*, Kunihiro Kashiwagi, Yasuhiko Yoshida, and Yoichi Murayama, Japanese journal of Applied physics, **1991**, *vol 30, no 8*, 1803-1807

[Kroe88] *Plasma deposition: Investigation on a new approach*, G.M.W. Kroesen, **1988**, Ph.D. Thesis, Eindhoven university of technology

[Lieb94] *Principles of plasma discharges and material processing*, Michael A. Lieberman, Allan J. Lichtenberg, **1994,** John Wiley & Sons, inc

[Lord57] *Infrared spectroscopy from 5 to 200 microns with a small grating spectroscope*, R.C. Lord and T.K. mcCubbin, Jr., Journal of the optical society of America, **1957**, *vol 47, no 8*, 689-697

[Luco83] G. Lucovsky, J. Yang, S.S. Chao, J.E. Tyler, and W. Czubatyj, Physical review B, **1983**, *28*, 3225-3233

[Marc90] *Fourier trabsforms in NMR, optical, and mass spectrometry*, A.G. Marshall, and F.R. Verdun, **1990**, Elsevier, Amsterdam

[Marr98] *Silicon hybride composition of plasma-deposited hydrogenated amorphous and nanocrystalline silicon films and surfaces*, D.C. Marra, E.A. Edelberg, R.L. Naone, E.S. Aydil, Journal of the vacuum science and technology A, **1998**, *16(6)*, 3199-3210

[Mitu99] *Deposition of silicon dioxide like films using an expanding thermal HMDSO/O_2/Ar plasma - An initial study*, Bogdana Mitu, **1999**, Internal report VDF/NT-99-06, Eindhoven university of technology

[Numa83] Y. Numasawa, K. Yamazaki, and K. Humano, Japanese journal of applied physics, **1983**, *vol 22*, L792

[Naka84] *Infrared absorption spectra and compositions of evaporated silicon oxides (SiO_x)*, M. Nakamure, Y. Mochizuki, and K. Usami, Solid state communications, **1984**, *vol 50, no 12*, p 1079-1081

[Pedr93] *Introduction to optics*, Frank L. Pedroti, Leno S. Pedroti, **1993**, Prentice-Hall International Inc

[Ragh01] *Infrared characterization of a cascaded arc plasma*, Ram Raghavan, Philip W. Morrison Jr., Journal of quantitative spectroscopy & radiation transfer, **2001**, *69*, 605-634

[Rauf97] *Argon metastable densities in radio frequency Ar, Ar/O_2, and Ar/CF_4 electrical discharges*, Shahid Rauf and Mark J. Kushner, J. Appl. Phys., **1997**, *82 (6)*, 2805

[Rich85] P.D. Richard, R.J. Markunas, G. Lucovsky, G.G. Fountain, A.N. Mansour, and D.V. Tsu, Journal of the vacuum science and technology A, **1985**, *3*, 867

[Stei86] *Diagnostics of low-pressure RF plasmas and the mechanism for polymer etching: a comparison of reactive sputter etching and magnetron sputter etching*, C. Steinbruechel e.a., IEEE transactions on plasma science, **1986**, *14 no 2*, 137-144

[Suga98] *Plasma etching - Fundamentals and applications*, M. Sugawara, **1998**, Oxford university press

[Thei94] J.A. Theil, J.G. Brace, and R.W. Knoll, Journal of the vacuum science and technology A, **1994**, *12*, 1365-1370

[Tomp93] *A user's guide to ellipsometry*, H.G. Tompkins, **1993**, Academic press, Inc, San Diego

[Verk92] *Binas*, G. Verkerk, J.B. Broens, W. Kranendonk, F.J. van der Puijl, J.L. Sikkema, C.W. Stam, **1992**, Wolters-Noordhoff Groningen

[Wilb91] *A wall stabilized arc as a light source for spectroscopic techniques*, A.T.M. Wilbers, **1991**, Ph.D. Thesis, Eindhoven University of Technology